Development of testing methods for the fatigue crack propagation in steel shot reinforced resins

An experimental and numerical approach towards a promising type of test and geometry for characterizing the fatigue crack propagation of SRR

T. Peeters

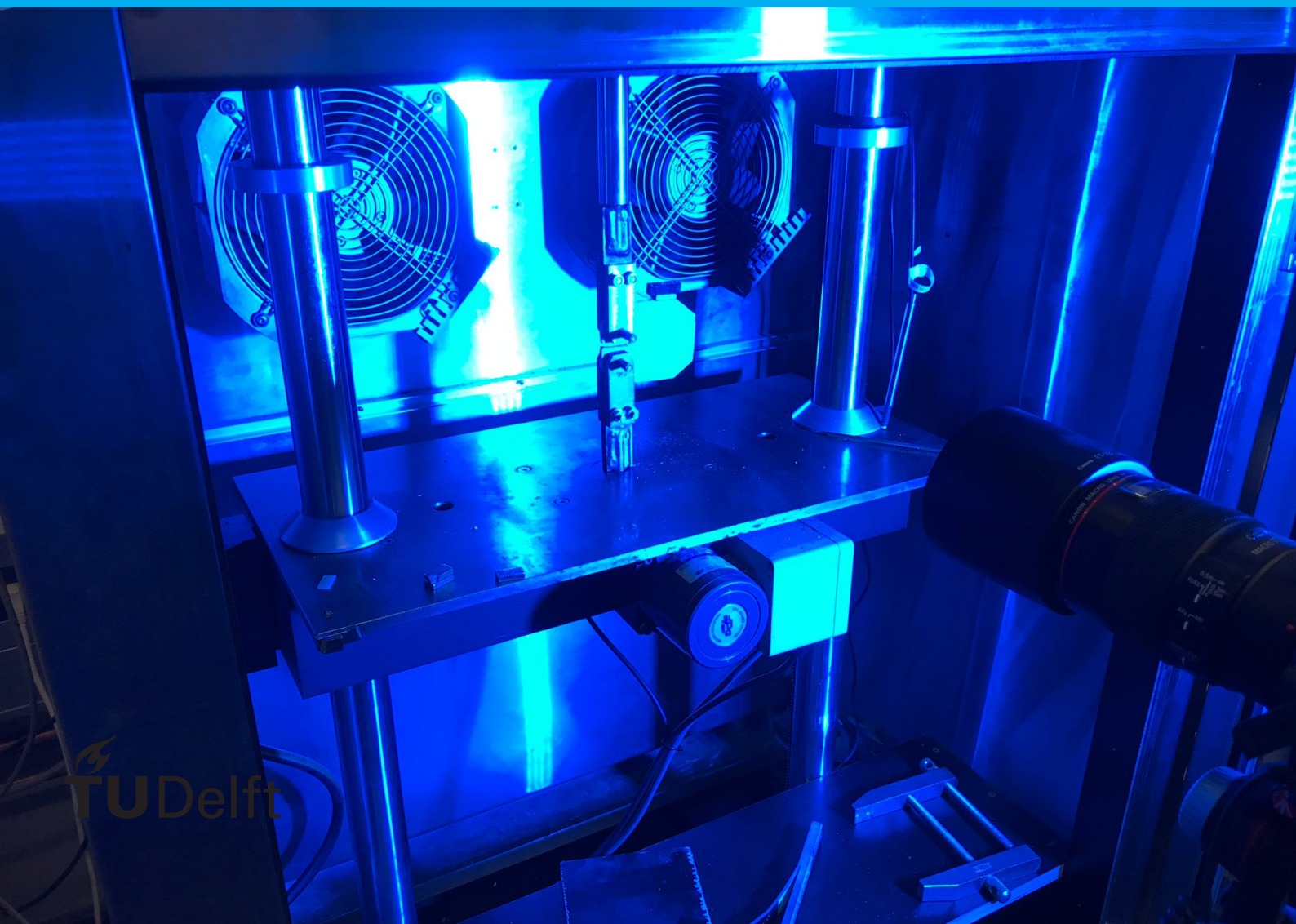

Development of testing methods for the fatigue crack propagation in steel shot reinforced resins

by

T. Peeters

to obtain the degree of Master of Science
at the Delft University of Technology,
to be defended publicly on Tuesday 23Th of August at 3 O'clock.

Student number: 4472934
Project duration: January 14, 2022 – August 23, 2022
Thesis committee:

Dr. Ir. M. Pavlovic,	TU Delft, Chair thesis committee
Ir. A. Christoforidou,	TU Delft, Daily Supervisor
Dr. Ir. K. Varveri,	Tu Delft, Thesis Supervisor

An electronic version of this thesis is available at http://repository.tudelft.nl/.

TU Delft

Preface

Somehow the hottest day of summer ended up the day I would write this nice part of the report. With it an amazing time at the TU Delft will come to an end. Working on the thesis had its ups and downs and I wont lie I am glad it is done. But, I did learn a lot during those ups and downs.

To give credit where credit is due. I definitely did not do this alone. Thus I would like to thank everybody that helped me along the way, large part is for my graduation committee for giving sharp insides and a notch in the right direction to propagate a bit further. I would like to thank Marko Pavlovic as chair of the committee for his helpful insights and concrete goals along the way. Angeliki Christoforidou as daily supervisor for her unending optimism, daily support and keeping me focused on the import parts. and Katerina Varveri for her knowledge on multi phase material crack propagation and having a critical second opinion. I would also like to thank John Hermsen as my lab supervisor for when I went 'hobbying' in the basements of Stevin-II and Giorgos Stamoulis for his guiding on the use of the testing machines in the lab, 'yes Giorgos, I think I believe that I did everything correctly.'

Well then something about friend and family. You probably know who you are. I would like to thank you all for hearing me out when I wanted to discuss anything or just complain about something taking longer than planned, but mostly for taking my mind of this work. Special thanks goes out for one specific whatsapp group that had to deal with all the picture, figures and results gathered, thanks for dealing with that provided amazing insights on those results. Lastly I would really like to thank everybody that helped me remove as much of the writhing mistakes as possible.

I guess that is it. It was an amazing student time and I am gone miss it, but it is time for the next adventure!

T. Peeters
Delft, July 2022

Summary

The increasing traffic load on highway bridges provides a need for replacement or improvement of the bridge decks. The design of a new bridge deck using fibre-reinforced polymer (FRP) bridge decks raises questions on the connection of a FRP bridge deck to a steel superstructure. At the Tu Delft a bolted connector injected with steel reinforced resin (iSRR) is developed for the connections between steel superstructure and FRP bridge deck. Steel reinforce resin (SRR) is a combination of steel shot (SS) and resin. The steel shot is added to achieve higher stiffness and reduce the total production cost. The iSRR connection can be produced using multiple methods. For all production methods, the SRR in the connector is produced by pouring SS around the bolt followed by the injection of the resin. The iSRR connector should accompany the fatigue resistance of the FRP bridge deck. A better understanding of crack propagation can help to increase the life expectancy of iSRR connections.

However, no standardized method for the testing of crack propagation in SRR exists. This research attempts to find a crack propagation testing method for SRR by investigating the use of compact tension (CT) and semi-circle bending (SCB) testing for the SRR material.

For the production 5 different casting methods were compared. From these methods, the closed mould injection casting and ring mould injection casting showed the most promising production method for the production of complicated forms in SRR. From this testing the need to use modified forms of CT and SCB was found, resulting in the use of a doubly tapered compact tension specimen (2TCT) and the design of the short tapered notched beam specimen (STNB). The modified specimen forms are tested under varying loading types. The 2TCT specimen is tested under load controlled, and displacement controlled loading. From this, the incremental increasing loading type was suggested. This loading type was used in the testing of STNB specimens. Lastly with the use of FEA the stress intensity factors for the modified test shapes were validated. The validation was done on the analytical formulas provided by literature for the unmodified shapes.

From this research, it can be concluded that the closed mould injection casting and ring mould injection both achieve good results for the production of complicated shapes with SRR. The incremental increasing displacement loading method leads to more stable crack growth. The 3 point bending testing type leads to the most promising results for crack propagation. With a linear correlation in the small range of K = 20-60 resulting in a Paris Law with $C = 4.3e - 7$ and $m = 2.41$.

It is recommended for further crack propagation testing to produce specimens with the least amount of voids. The voids are expected to have a high contribution to the big spread of data found during the testing. For better insight, the voids in the tested specimens could also be investigated.

Contents

1 Introduction

1.1. Motivation and problem statement

In the Netherlands many bridges build in the 60's and 70's are now reaching the end of their life span. The predominating problem in these bridges is the bridge deck. These bridge decks were not designed to cope with the increase in traffic load that occurred in the last 60 years. Thus, they need to be replaced or renovated. [5]

Solutions are found in reinforcing the bridge, by among others, high strength concrete, superglue or fibre reinforced polymer (FRP), or in replacing the bridge deck in severe cases. In the scenario of replacement, the bridge deck can be replaced by a FRP bridge deck. Due to the lightweight, fatigue and corrosion resistance properties of FRP these bridge decks could be a desirable solution for the problem. However, the connection between the FRP bridge deck and the steel superstructure poses some difficulty. The FRP to steel connection could be performed using 3 different main ideas: bolted connection, bonded connection, or grouted connections. [33] All of the mentioned connections have different pros and cons. At the TU Delft research on the design an iSSR bolted connection is performed.

From this research the following designs is proposed by A. Christoforidou, see figure 1.1. The design uses a relative unknown composite material, steel reinforced resin (SSR). The SRR exists of steel shot and sheet moulding compound (SMC) resin Daron 8151. The steel shot is used to improve the stiffness of the resin and make production less expensive. The SRR is used in the connection to reduce the damage on the FRP bridge deck due to preloading of the connection. The preloading will increase the fatigue life span of the connection if the SRR can withstand the fatigue loading. Research on the behavior of cyclic compression-compression loading and compression damage is already being conducted [36],[55]. also, the fatigue strength in tension is being researched. However, the crack propagation in tension and shear in SSR is still unknown, and because no standardized test setups exist for this sort of composite material, this cannot be tested easily. Finding a suitable method for determining the propagation of the crack can lead to an increased lifetime of the connection in case of a found crack. Even back in 1989 K. Tanaka has already concluded that both experimental and theoretical studies are necessary to understand fatigue crack propagation in new advanced structural materials [49].

1.1.1. Main objective

This research is focusses on finding a cyclic crack propagation test setup, based on already existing standardized test setups, for SRR. This will be done according to theoretical background on standardized materials and their crack propagation, finite element models (FEM) of SRR test setups and laboratory tests using the SRR applied in the iSSR connector. From this the easiest, most accurate and consistent test setup will be proposed as setup to further research of the crack propagation and fracture mechanic parameters.

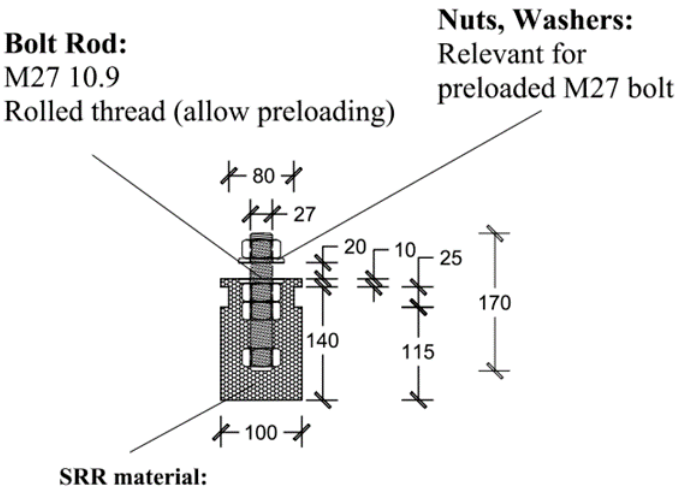

Figure 1.1: Design connection FRP bridge deck to steel superstructure proposed by A. Christoforidou

1.1.2. Research question

The following main research question comes from the main objective:

- Which is an appropriate type of test and type of loading to study fatigue crack propagation of the Steel Reinforced Resin (SRR) material?

With the following sub-questions:

- How does the micro structure of the SRR material compare to that of steel, concrete, and asphalt?

This sub-question focuses on the theoretical difference between the materials and the crack propagation of the materials, giving more insight on the expected test results and a better indication for suitable test setups.

- Which are the expected crack propagation paths in SRR?

This sub-question focuses on understanding of the crack propagation in the test setups and FEM. Including the material micro structure of steel, concrete, and asphalt and crack propagation paths in those materials. The expected crack propagation paths can be visualized to give more inside on the crack propagation found in the testing setups.

- What are the material parameters and formulation of Paris law in an XFEM for numerical simulation of fatigue crack propagation in the SRR material?

This sub-question focusses on the numerical simulations of SRR to use the FEM to predict crack propagation in different configuration when working with SRR.

1.1.3. Research methods

The study will focus mainly on experimental data of two test methods based on asphalt, concrete, and steel tests: semi-circle bending test (SCB) and compact tension test (CTT). In the event of unexpected results, other tests are set as backups. The parameters that are variable for the different test setups are size, temperature, and loading speed. The SRR mixture will remain constant for all specimens. The experimental date will be supported by literature study for sub question 1 and 2. Sub question 3 will combine literature study, with experimental adopted material properties to simulate the crack propagation in the FEA package Abacus. The same simulation can be performed using other FEA packages that have access to XFEM.

1.1.4. Report outline

In chapter 2 the state of the art knowledge of subject relevant to the testing of crack growth rate in SRR and the modelling of those tests will be discussed. This information is used to make educated decisions during testing and modeling.

Chapter 3 reports on the ways of producing possible SRR specimens within the limitations of the material and the lab, how this production method is improved during the research, and what the expected effects of the production methods are.

In chapter 4 the results of the CT tests will be reported. A small remark will be made on initial static tests, but the focus is on fatigue tests and the chances between tests to improve the results.

In chapter 5 the results of the 3-point bending tests will be reported. Again, a small remark will be made in the initial static SCB test. The focus will be on the results of the TNB fatigue testing.

In chapter 6 the numerical model decisions and results will be represented. Furthermore, the numerical model results will be compared to the test results reported in chapter 4 & 5.

In chapter 7 the conclusions on the research questions provided by the knowledge reported in the previous chapters will be drawn. Next to that some recommendations for further research will be provided.

Finally in chapter 8 a small discussion on the process and reporting of the thesis will be given.

2

State of the art

2.1. Paris Law

One of the most well-known methods to define crack propagation is the Paris Law. This method was first suggested by Paris and Erdogan in 1963. It gives the growth rate of a crack in stage II. Stage II describes the stable growth of a crack larger than 1 mm. This growth rate is given as a function of the stress intensity range in one load cycle. This gives the following equation.

$$da/dN = C(\Delta K)^m \tag{2.1}$$

- a = crack lenght
- N = the cycle number
- da/dN = the crack growth per cycle
- ΔK = maximum stress intensity factor - minimum stress intensity factor
- C and m are material coefficients depending on environment, frequency and stress ratio

The Paris Law is only applicable in linear elastic fracture mechanics, under tensile loading, and for long cracks. Because of the power law relationship of the Paris Law it will give a linear graph on a logarithmic plot. See figure 2.1 for a typical fatigue crack growth graph.

In the graph, a threshold stress intensity range can be found. The reason for this occurrence is quite complicated. One of the explanations for it is that due to the compressive stress induced by the plastic wake the crack tip is shielded and no plastic deformation occurs. Another explanation is that

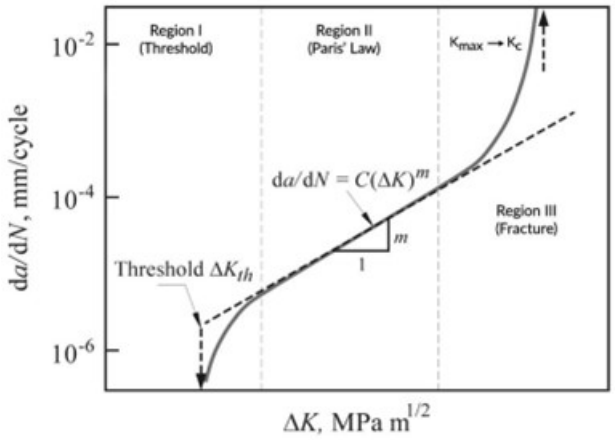

Figure 2.1: Standard Paris Law curve ([17])

the plastic deformation of the crack tip cannot penetrate micro structural barriers in the material. The minimum stress intensity can reach negative values which will lead to crack closure, because there are no established conventions to take into account the crack closure it is advised to avoid this. However, if it does take place the full range can be taken into account or only the tensile part of the cycle ([16]).

2.2. Fatigue damage modelling

2.2.1. Linear Elastic Fracture Mechanics

Traditionally linear elastic fracture mechanics (LEFM) is used for fatigue crack modelling. LEFM is a restricted method because of the small-scale yielding compared to the crack length. Therefore, it can only predict the stress state close to the crack tip if the fracture process zone is very small. Using the LEFM theory in FEM requires refinement of the mesh near the crack tip to account for the small-scale yielding. This refinement needs to move along with the crack propagation, thus using a lot of computation time. In heterogeneous models this is even more the case because of the complexity of the crack propagation path.

2.2.2. Cohesive Zone Method

The cohesive zone Method (CZM) attempts to eliminate the need for mesh refinement around the crack tip by seeing crack propagation as a gradual occurrence in which the separation takes place across an extended crack tip and is restricted by the cohesive traction. From which it lends its name. Because of the gradual occurrence the CZM can predict the behaviour of uncracked material, there is no need for a significantly small nonlinear zone in the model and no initial crack is needed. This makes CZM a popular method for bi-material interface when the interface can be pre-defined. In concrete and asphalt this is normally the case.

2.2.3. eXtended Finite Element Method

As the name suggest the eXtended Finite Element Method (XFEM) extends the classical finite element method by enriching the solution space to differential equations with discontinuous functions. With this, it can simulate the crack propagation without the need for remeshing. The advantage that XFEM has over LEFM and CZM is that no predefined-crack path or initiation is needed and no special element are needed in the interface for crack development.

The solution space is enriched by the discontinuity function $H(x)$ and the asymptotic function $F_a(x)$. The discontinuity function represents the gap between the crack surfaces and the asymptotic function the singularity around the crack tip.

2.2.4. XFEM in Abaqus

Crack propagation analysis Abaqus allows the uses of fatigue crack growth criterion in general fatigue crack growth approach and direct cyclic approach. The former is used in brittle linear materials and the latter in ductile materials. The onset and crack growth are characterised using the Paris Law. In the software the Paris Law is defined as the relative fracture energy release rate to crack growth rate instead of the more standard definition of stress intensity factor to crack growth rate. The fracture energy release rates are calculated based on the virtual crack closure technique (VCCT) [43].

The beginning of fatigue crack growth is characterised by ΔG and is defined as shown in equation 2.2.

$$f = N/(c_1 * \Delta G^{c_2}) \geq 1 \tag{2.2}$$

If nothing is specified about the onset Abaqus assumes that the crack is always allowed to grow. The growth rate of the crack is given by equation 2.3 if $G_{thresh} < G_{max} < G_{pl}$.

$$da/dN = c_3 * \Delta G^{c_4} \tag{2.3}$$

where c_3 and c_4 are material constants. To relate c_3 and c_4 to the general used Paris law constants C and m equation 2.7 can be substituted in equation 2.1 to find the relations shown in equation 2.4 and 2.5.

$$c_3 = C * E^{m/2} \tag{2.4}$$

$$c_4 = m/2 \tag{2.5}$$

The direct cyclic approach allows the user to apply a force following a cyclic loading sequence to obtain the stabilised response of a structure. Abaqus uses Fourier series and time integration to obtain the stabilised response.

2.3. Fatigue crack propagation testing methods and specimens

In fatigue crack propagation testing the goal is to produce a stable crack growth to find the da/dN and ΔK to establish the Paris Law parameters. During the testing, the length of the crack can be found with visual direct methods and measurable indirect methods. The visual methods can be done by traveling microscope or digital image correlation (DIC). The traveling microscope measures the crack length by following the crack tip with a cross-hair microscope and finding the vertical displacement of the microscope. This method needs a crack that is visually easy to follow ([41]). DIC uses random and unique blocks of pixels on the surface of the test specimen to find the surface deformation of the specimen. Using these deformations, the crack location can be found ([28]). For the indirect method distance measurements between measurable point are correlated to the crack length. Thus, this method uses formulas found in research to give a best estimate to determine the crack length during testing.

The stress intensity factor, ΔK, depends on specimen geometry, the crack length, and the force range.

$$K = Y * \sigma * \sqrt{\pi/w} \tag{2.6}$$

- $Y = f(a/w)$

This means that every geometry has a different geometry dependant function that in most test cases is found using numerical methods, as very few closed form solutions exist. FEM is the most popular method as other methods include experimental and semi-theoretical methods. The stress intensity factor has a direct relationship to the energy release rate and J-integral. In some research fields energy release is preferred over the stress intensity factor. for pure mode 1 and mode 2 loading in plane stress conditions the relation is strait forward, see equation 2.7

$$G_I = K_I^2(1/E) \tag{2.7}$$

$$G_{II} = K_{II}^2(1/E) \tag{2.8}$$

To indicate proper fatigue testing methods, it is imported to first clearly indicate the different testing methods possible and their pros and cons. Institutes such as ISO and ASTM have standardised methods for testing tension-tension crack propagation. These methods not only give specific requirement for various specimen configurations but also give recommendation and requirements for fatigue crack growth rate testing. Other methods found in literature are also represented to provide more specialised methods that tackle different cons of the standardized methods.

2.3.1. Compact tension test

In compact tension specimen a single edged notched specimen is loaded on two pinned points in tension. The form of the specimen makes it possible to produce pure tension in the crack path. CT specimens are regulated according to ISO and ASTM E647 [47] standards. See figure [] for the ASTM standard ct dimensions.

The stress intensity factor for CT specimens can be calculated using the formula found in the ASTM E647.

$$\Delta K = (\Delta P)/(B * \sqrt{W}) * (2+\alpha)/(1-\alpha)^{3/2} * (0.886 + 4.46 * \alpha - 13.32 * \alpha^2 + 14.72 * \alpha^3 - 5.6 * \alpha^4) \tag{2.9}$$

- Where $\alpha = a/W$; valid for $a/W => 0.2$

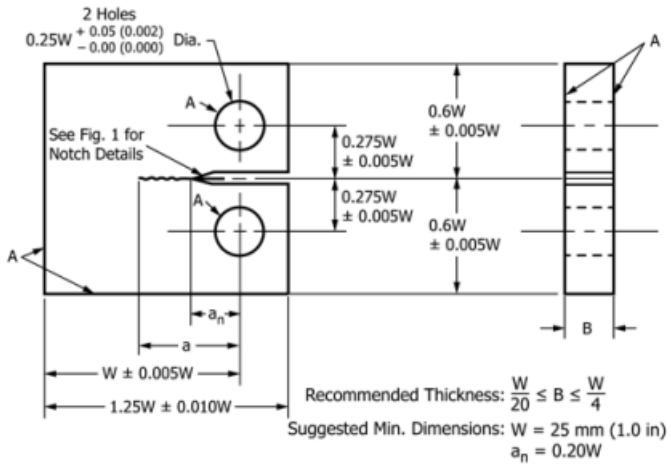

NOTE 1—Dimensions are in millimetres (inches).

NOTE 2—*A*-surfaces shall be perpendicular and parallel as applicable to within ±0.002 *W*, TIR.

NOTE 3—The intersection of the tips of the machined notch (a_n) with the specimen faces shall be equally distant from the top and bottom edges of the specimen to within 0.005 *W*.

NOTE 4—Surface finish, including holes, shall be 1.6 µm (63 µin.) or better. A surface finish of 0.8 µm (32 µin.) or better on the specimen faces may provide a better surface for making optical measurements of the crack.

Figure 2.2: ASTM Standard CT specimen

CT specimens use little material to provide a long possible crack path. Therefore, they are extensively used in steel fracture mechanics. In other materials the complex form of the CT specimen makes it harder to use or the material specifications lead to extra failures to occur alongside the crack growth. This leads to modification on the CT specimen or other specimen forms to be dominated in those areas. An indication on some of the modifications on the CT specimen are presented here.

Mini CT
The mini CT (Mini-CT) specimens are CT specimens who's dimensions are approximately 4 x 10 x 10 mm. The Mini-CT are useful when dealing with precious or hard-to-come-by material. However, they do come with problems of accounting for size effect, using small specimen data for large structures and small allowed crack length growth [44].

Disk-shaped CT
The disk-shaped CT (DCT) and modified disk-shaped CT (MDCT) are both used in asphalt concrete and concrete to be able to test already existing structures. The disk shape of the tests makes the form easy to obtain by drilling cylindrical cores [52]. The modified disk-shaped CT uses re-bars instead of the normal loading holes to load the specimen. This reduces the risk of premature failure around the loading holes [12].

Doubly-tapered CT
The doubly-tapered CT (2TCT) is advised by [10] to be used in laminated composites. The 2TCT significantly reduced the chance for compression failure to occur in the upper and lower edges of the specimen during testing. Furthermore, the double tapering also reduces the compression failure in the right edge. However, it does give a higher chance for global instability and failure around the loading holes to occur in the test.

2.3.2. Notched beam specimen test
The notched beam specimen gives a flexible specimen configuration. This leads to options of easy investigation of e.g. size effects and mix-mode behaviour. The simple loading configuration makes it a test form that can be easily replicated in many civil engineering labs [35]. The notched beam specimen

is mostly used in concrete, asphalt concrete and rock testing [54]. Where the flexible configuration give many options for pouring and cutting of the specimens. It does need rather large dimension before an ideal possible crack length is achieved. Especially in concrete and asphalt concrete where the fracture process zone depends on the aggregate size [40]. Together with the difficulties facing in use material testing in this configuration this led to the development of the Semi-circle bending test.

Semi-circle bending test
The semi-circle bending specimen (SCB) is a 3-point bending test on an arched specimen. Even though it is also a notch specimen under 3-point bending, it is generally considered to be a different form than the NB specimen. The specimens are generally produced from a cylinder core, where discs are sawed off. The disc will be cut in half and a notch is created in the middle of half a disc. Other production methods are also possible, but the main one makes SCB a good method for testing in use material. This, along with the simple geometry, loading configuration, and straightforward testing procedure it shares with the NB specimens, makes SCB a highly discussed testing method. However, the SCB has a difficult stress distribution compared to the NB [35]. Due to the stress distribution, a dimensionless K formula is harder to find. Some attempts have been made to find a dimensionless K formula [26], [51], [6]. But no standards have been made for this. The most widely used dimensions are $r = 150mm$ and $S = 120mm$ or $r/S = 0.8$. For those equation 2.11 shows the dimensionless factor for SCB shown by [26].

$$K_{I\_SCB} = (P_{max} * \sqrt{\pi * a})/(2 * R * B) * Y_I \tag{2.10}$$

$$Y_I = 4.782 - 1.219(\alpha/r) + 0.063 \exp 7.045(\alpha/r) \tag{2.11}$$

2.4. Material structure state of the art materials and their link to crack propagation

2.4.1. Metals

The material structure of metals, or more commonly look at as ductile material, is one of the most well-known structure. The main focus will thus lie on the mechanics of crack propagation in regular ductile materials. But a small introduction of the material structure will be provided.

The material structure of metals is made out of individual crystalline areas, commonly referred to as grains. The structure, size, and orientation are the result of the material composition and the way the material is made. The structural characteristics are directly related to these grains. Inside the crystalline areas, irregularities can be found. These irregularities are known as dislocations. The dislocations inside a metal grain are allowed to move because of the relative free sliding of atoms in metallic atom structures. When dislocations move, they commonly end up at the boundaries of the crystalline areas. In addition, when a metal is deformed, new dislocations are generated. The increase dislocations and accumulating of dislocations gradually increases the resistance to deformation. This causes hardening of the metal and is known as strain hardening, making the metal harder to deform, but also more brittle and prone to failure.

For a good understanding of the factors that influence the crack growth rate of ductile materials, it is good to know that crack growth is promoted by intrinsic microstructural damage and restrained by extrinsic mechanisms that act behind the crack. Intrinsic microstructural damage in ductile material is usually seen as the creation of voids and micro cracks due to the sharpening and blunting of the crack tip. This causes dislocations to accumulate and toughening of the material around the high-stress region before the crack. This causes micro cracks. The extrinsic mechanisms can be divided in three groups: crack deflection and meandering, zone shielding and contact shielding. Figure 2.3 shows a good illustration of the different extrinsic mechanisms. In ductile material, the physical contact between the two crack surfaces is the main extrinsic factor [39].

The intrinsic mechanisms are inherent to the material, thus are independent of the crack length or the geometry of the specimen. For example, under monotonic loads the intrinsic mechanisms control the stress intensity needed for initial cracking. Extrinsic mechanisms act in the crack wake, thus they are dependent on the crack length and the geometry. These mechanisms will mainly govern the crack growth. The extrinsic mechanisms are the cause of the development of the R curve behaviour, where

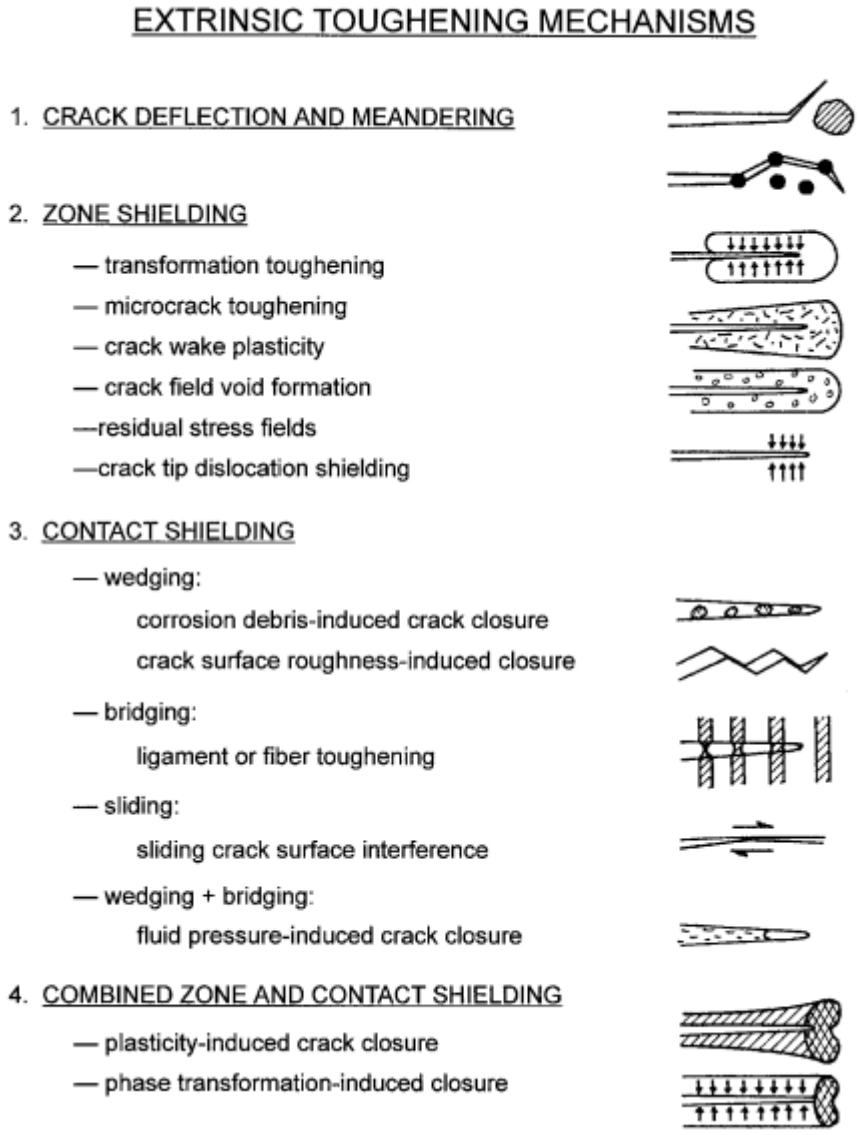

Figure 2.3: Schematic illustration of extrinsic toughening mechanism [38]

depending on the material and the geometry the crack growth rate can decrease with an increase in stress intensity. The intrinsic and extrinsic mechanisms depend on different properties of the material structure.

So, in ductile materials the crack propagates from the crack tip where in the high stressed zone deformation take place, causing this part of the material to undergo strain hardening. The crack will propagate through the grains. Twisting or kinking of the grain angle along the crack path increases the resistance to crack propagation [24]. But when looking at the Paris region of the crack propagation, these effects are negligible according to literature study done by [20] on Martine steel. According to the same study the crack diversion, crack bifurcation, and metal crumb formation are micro structure depending properties that do influence the crack propagation in the Paris region of the crack. However, research on ultrafine-grained steel shows that the there the grain size and orientation does influence the crack growth rate and threshold values [31]. Therefore, it seems that the fines of the steel grain have a large effect on which material structure affects the crack propagation in metals.

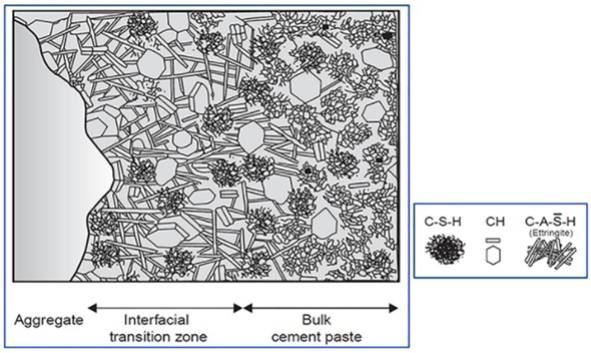

Figure 2.4: schematic diagram of ITZ in concrete, [18]

2.4.2. Concrete

The work by [18] gives a good idea of the material structure of concrete and the effects on the crack propagation. Concrete can be considered to have three phases: Cement paste, aggregate, and the interfacial transition zone (ITZ) between the former two. The paste consists mostly of water and a binder, most commonly cement, other supplementary materials can also be used to improve the paste properties. The following phases can be found in cement paste: calcium silicate hydrate (C-S-H), calcium hydroxide (CH), ettringite, monosulfate, unhydrated cement particles, and air voids.

The interfacial transition zone between the cement paste and aggregate is a part of the cement paste where the structure of the cement is different than in the normal cement paste. In the interfacial transition zone less unhydrated cement, less calcium silicate hydrated, large crystals of calcium hydroxide, greater concentration of ettringite and a higher porosity can be found than in normal cement. See figure 2.4 for a schematic indication of this ITZ.

The ITZ effects the stiffness and strength of concrete due to its lower density and strength. The first microcracks in concrete occurring here, caused by the lower strength and stress point of stress concentration around the aggregate. The bond strength between the paste and the aggregates is influenced by the shape, size, mineral composition surface roughness, surface moisture, porosity of aggregates and the water/cement ratio. These factors all effect the interfacial transition zone and the bonding between the cement and aggregates. Concrete mainly gets its strength from the adhesion between the solid parts of hydrated cement pasta. This adhesion exists because of the Van der Waals forces, which depend on the size and nature of the solid parts and the adhesive capabilities.

The development of bond cracks at mortar aggregate interfaces is an important factor in the inelastic deformation and fracture behaviour of concrete. Cracks in normal strength concrete often propagate along the interface between the mortar and the aggregate, absorbing energy before linking and forming continuous cracks through mortar at failure. This results in the quasi-brittle behaviour of normal concrete. In high strength concrete the interfacial transition zone are more dense and stronger and thus the concrete acts more brittle.

The paper by [37] shows that when concrete is loaded until failure, it indeed acts semi-brittle. The behavior under cyclic tension loading shows indeed that the deformation is partly reversible, but the irreversible part increases greatly with the increase in deformation. The study done by [23] shows that concrete has two stages in its fatigue crack growth rate, a decreasing growth rate stage followed by an increasing growth rate stage. Here the second stage can be modelled using the Paris Law. Two competing mechanisms influence these different stages, namely the increase in resistance due to the rising R-curve and the increase in K due to the increasing crack length. Here, the extrinsic mechanisms of concrete are therefore bigger at the start of the crack growth than the increase in stress intensity. The concept of the R-curve shows that the energy required to increase a crack in length increases over the crack length. In an infinite-sized specimen this keeps increasing, where a finite size specimen has a upper limit, because the different extrinsic mechanisms reach their maximum contribution.

2.4.3. Asphalt

Asphalt concrete is also seen as a three phase material, aggregates, fine aggregate matrix (FAM) and the ITZ [56]. The FAM phase consists of asphalt binder, air voids, fine aggregates, and filler

material. Together with the ITZ it acts as the primary phase for the damage and deformation of the complete mixture. In this, it has much in common with concrete. The same damage evolution in the microstructure is also found. However, the FAM phase has visco-elastic properties greatly influencing the fatigue resistance of the material. Many methods to investigate the fatigue damage accounting for this visco-elastic properties exist [9]. A typical assumption for asphalt concrete requires the minimum specimen dimension to be at least three to four times larger than the maximum aggregate size to ensure that the experimental results are statistically valid. This is due to the fracture process zone in quasi-brittle materials [21].

2.4.4. Resins

Here mainly epoxy, polyester and vinylesters are looked into. All the mentioned plastics are made out of polymers chains. The polymers are mixed with a hardener to cure the mixture. This process takes place on a molecular level and exist of the cross linking of the polymers. The result is a permanent change to the microstructure of the plastic. Curing of these resins is an exothermic process. The amount of cross-linking and flexibility of the polymer chains influences the thermo-mechanical properties of the resin. The resins can vary from brittle to ductile behaviour depending on its properties and will behave more brittle under cyclic loading due to its strain rate dependency [36]. All resins have a glass transition temperature. When a material reaches such temperature, it will act rubbery, soft, and flexible; the cross-linking prevents free flow. The resin can be seen as a viscous material in this phase [50].

Polyester resin contains double covalent bonds in its polymer chain and is produced by free-radical polymerization. Epoxy resin is produced by condensation polymerisation [7]. Vinylesters are a hybrid form of polyester resin that is strengthened by epoxy resin. This gives much more freedom in achieving the desired properties. Generally, epoxy resins are stronger, have a higher glass transition temperature, have good moisture resistance, and better thermo stability than polyester resins. Polyester resins are however cheaper and easier to work with. Vinylester resins can combine desirable properties of polyester and epoxy resins [1].

The effect of the microstructure on the crack propagation can not be clearly indicated. However, research done on the crack propagation properties by M.J Owen and R.G. Rose shows that the crack growth rate in polyester resin was independent of the resin flexibility. Post microscopic examination shows that the stable crack growth region increases with increasing resin flexibility [34]. Because of the nominally homogeneous nature of resins, the same standards as for steel can be used. S. A. Sutton showed that for epoxy resin, a much higher M is found in comparison to normal metals. He also indicates that the main cracking mechanism in epoxy could be cleavage like or branch cracking [48]. J. Karger-Kocsis and K. Friedrich add to this that in multiple toughened epoxy resins the microcracks density ahead of the crack tip have the most influence on the fatigue failure [22]. Research on two sets of resins (Epon 815/ Versamid 140 resin and Epon 828/Epon resin) under tensile-tensile cyclic loading was done by L. Lorenzo and H.T. Hahn [27] to find the effect of ductility on the fatigue behaviour of epoxy resins. The fatigue strain for ductile resin was found to be 27% higher than of brittle resin. Plastic deformations were observed for both the resin specimens with the permanent strain being three times larger for ductile resin. The decrease in creep strain was greater for the brittle resin. The brittle resin failed in one crack without stable crack growth, where te ductile resin showed crack initiation, propagation, and crack failure.

2.5. Steel reinforced resin

2.5.1. Material structure

Steel reinforced resin is a composite made up of steel shot and resin binder material. The steel shot follows normal steel parameters. Epoxy resin, vinyl ester resin, and unsaturated polyester combined with polyurethanes are used in previous research on SRR as binder. ([32], [11]). The resins have varied parameters. The resins all have strain-rate-dependant stiffness; the impact of these effects still depends on the specific resin used. The materials thus lead to a combination of a relative stiff materials as filler material and a strain rate depending resin as binder, comparable to that of (asphalt) concrete. The main difference in the structure is in the size and angularity of the filler material. Research done by J. Wang on the effects of different material structure parameters of asphalt on fracture modelling shows that angularity of aggregate influences the initiation of crack. The lower the angularity the higher force needed for initial cracking. Furthermore, the maximum size of the aggregate has a negative correlation

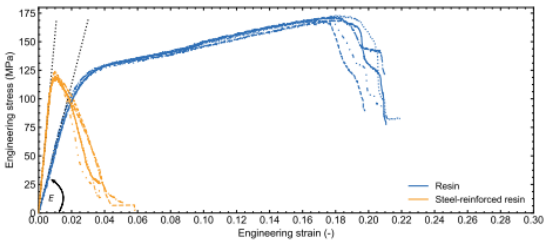

(a) RenGel SW 404 + HY 2404

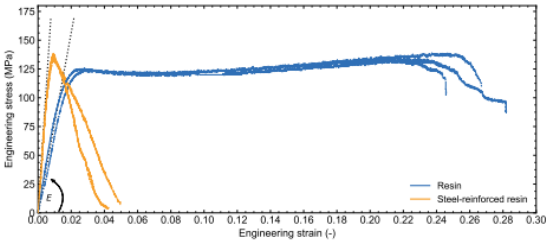

(b) RenGel SW 404 + HY 5159

Figure 2.5: cylindrical compression tests results done by [32]

the initiation of the crack [53]. The materials have a large difference in parameters from that of asphalt concrete. With both the steel shot and the aggregate having a higher strength than their respective binder material, this will not be a factor in the strength difference. However, the binder materials show a large difference in strength, stiffness and viscosity. The development of damage in SRR is mainly due to the plasticity of resin and interface damage [55].

2.5.2. Static behaviour of steel reinforced resin

M.P.Nijgh[32] did experimental research on two epoxy resins: RenGel 404 with hardener HY 2404 and RenGel 404 with hardener HY 5159 with steel shot of size class s330. The SS was assumed to be in loose random packing resulting in a volume fraction of 60% SS. The experiments were done on cylindrical specimens loaded under uniaxial compression under confined and unconfined conditions. For this study, the unconfined tests are the most interesting. The SRR specimens show a significantly higher Young's Modulus than the pure resin specimens. The increase in Young's Modulus was concluded to be proportional to that of the increase in Yough's Modulus of the resin. The strain hardening found in the NY 2404 resin seemed to have little impact on the SRR using the same two component resin. Drucker Prager parameter was then found to have agreement between the experimental results and FEM's.

Material	Associated flow			Non-dilatant flow			Elastic	
	β	κ	ψ	β	κ	ψ	E	ν
Resin, RenGel SW 404 + HY 2404	10.33°	0.93	10.33°	10.70°	1.00	0.00°	5640	0.315
Resin, RenGel SW 404 + HY 5159	10.33°	0.93	10.33°	10.70°	1.00	0.00°	7818	0.315
Steel-reinforced resin, RenGel SW 404 + HY 2404	38.30°	0.78	38.30°	39.44°	1.00	0.00°	15700	0.22
Steel-reinforced resin, RenGel SW 404 + HY 5159	35.74°	0.78	35.74°	36.54°	1.00	0.00°	21900	0.22

Table 2.1: Model parameters used by [32]

3

Specimen production

Steel reinforced resin is a difficult material to process. The steel reinforced resin has a large difference between stiffness of the resin and the steel shot and relatively low binding between the two. This can make machining the material result in irregularities on the surface, due to steel shot releasing from the surface during machining. The spread of material parameters in the production of SRR makes it important to reduce spread in dimensions and resin as much as possible. This is why consistent blending and casting is important. Four main goals were set for the production method:

- A repeatable process.
- A consistent process.
- A final specimen that is representative for the intended use case.
- Minimisation of imperfections found in the final specimen.

3.1. Production methods

During the project different production methods were considered and attempted. Results from these attempts were combined to come up with the final production method. To give a good understanding on the production process, all the attempts will be discussed briefly. Because of the problems discussed in the chapter 2.5 casting was the chosen production method of the test specimens. Methods such as high pressure casting and vacuum casting were not considered due to limitations of the facilities available in the STEVIN-II lab.

The first decision to make is the choice of mould material. Timber, steel and silicon rubber are commonly used mould materials. The materials each have different strengths and weaknesses, see table 3.1. Important criteria for the mould are the following:

- Chemical resistance: The resistance of the materials to other chemical substances. Important for the effect of the resin on the mould
- Heat resistance: the resistance of the material to heat. the curing heat of the SRR should not effect the material. Higher heat resistance retains the option for oven curing
- Releasability: The ease with which the specimen can be released from its mould. difficulty in releasing can result in specimens breaking during demoulding or residual SRR being left in the mould.
- Indentation: The amount the material can deform by force. The high self-weight of the SRR can indent the mould and influence the accuracy of the test specimens.
- Accuracy: The possible accuracy that can be achieved with the material. Higher accuracy lead to less deviation between the test specimens.

- Reusability: the resistance to degradation of the material due to use of the mould. Better reusability means more specimens can be produced before the mould has to be replaced
- Production: The ease of producing moulds with the material. Materials that are easy to work lead to shorter production time and allow the production of complex shapes.

Based on these criteria silicon rubber was chosen as mould material. This was mainly for its high chemical resistance and good releasability while still providing moderate accuracy and reusability. To reduce the problem of indentation a high stiffness silicon rubber is used in the form of Silicones Addition Transparent 40 Normal. See [15] for the complete product info.

Material	Chemical resistance	Heat resistance	Releasability	Accuracy	Reusability	Indentation	Production
Timber	–	+-	++	-	+-	+	++
Silicon rubber	++	+	+	+	+	-	++
Steel	+	++	–	++	++	++	–

Table 3.1: mould material comparison

Five methods of casting were tried during the project. Here the observations on the 5 methods will be presented along with the advantages and disadvantages of these various methods.

3.1.1. Open mould casting

A high mould was filled with steel shot up to the required height of the test specimen. Then resin was added to achieve the desired weight ratio between the steel shot and the resin. To even out the top surface and reduce the air content of the specimen, the specimen was put in a shaker. See figure 3.1a for a illustration of open mould casting.

Open mould casting is an easy production method with great flexibility on specimen thickness and SS to resin ratio. It does however leave one surface rough and can lead to high fluctuation of specimen thickness (about +- 0.5mm in one specimen). In the ASTM standard it is advised against using specimens with rough surfaces as this could cause artificial influence on small crack growth behavior. The thickness fluctuation would greatly effect the stress intensity factor. Taking the exact thickness into account at the position of the crack tip would greatly increase the computational difficulty of the test. For these reasons the open mould casting was not chosen as a final production method.

3.1.2. Premixed open casting

In this method the focus was on reducing imperfections and making the SS to resin mixture as consistent as possible. To achieve this the SS and the resin where mixed before casting. This gave high flexibility in the volume ratio of SS to resin, made coating the SS with resin easier and gave to option to extract air voids by vacuuming the mixture before casting. These factors greatly improved the consistency of the mixture. However, during casting the high viscosity of the mixture made producing flat surfaces almost impossible, leading to the same problems as with the open mould casting but to an even higher degree. A method to prevent this could be casting with excessive resin to increase the workability of the mixture. Because this excessive resin has to be removed afterwards in order to not impact the testing results this was not tried. See figure 3.1b for a visualization of this method.

3.1.3. Closed mould casting

For this method a completely enclosed silicon mould or a silicon mould with a cover-plate can be used. Again the mould is first filled with SS. The resin is poured from one central point. The high viscosity of the resin made the pouring take longer than the pot life of the resin. This resulted in some parts of the specimen not being filled with resin, see figure 3.1c. As a result of the central pouring hole there is some excess material on the specimen. This is later removed with a grinder. This does leave a rough surface at the point of pouring. The pouring of the resin also reduces the flexibility with the SS to resin ratio because it depends on how the resin fills the mould. The enclosed mould did however, succeed in producing a specimen with two smooth surfaces and no fluctuation in thickness.

3.1.4. Closed mould injection casting

The closed mould injection casting method uses the same mould principles as the closed mould casting. However, in this method two tubes are put into the mould when the SS is added. The resin is then

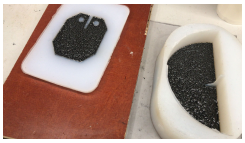

(a) Open mould casting

(b) Premixed open casting

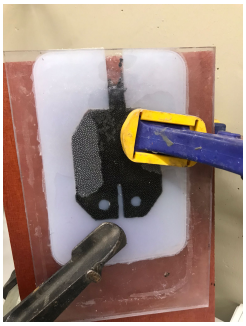

(c) Closed mould casting

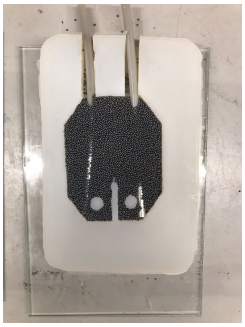

(d) Closed mould injection casting

Figure 3.1: Different casting methods

injected into the mould through the two tubes to fill the mould from the bottom, moving the tubes up when the resin level rises. Two tubes are needed to ensure resin is evenly distributed at both sides of the notch. The tubes are then removed, which causes the SS level to drop. Within the pot life of the resin SS is added from the two injection holes. The interlocking of the SS can leave a V-shaped pure resin part between the injection holes.

The method is material intensive because the tubes and ejectors are hard to properly clean and need to be replace often. It does however produce smooth specimens with proper distribution of resin and with a presentable material consistency to the real life scenario where the resin is also injected under pressure from the bottom. As with the closed mould casting, the flexibility in the SS to resin ratio is rather low and the extensions do need to be removed.

3.1.5. Ring mould injection casting

Ring mould injection casting is a small modification to closed mould injection casting. Instead of a mould with a cover-plate, a ring with two cover-plates is used. This method can only be used for specimens without holes. However, when used it produces two identical surface finishes, great control on thickness when using spacers and easy demoulding, even without using a flexible mould. This would mean that steel moulds could be used for this method to take advantage of the higher accuracy and reusability of steel. During production with this method only silicon rings where made. The flexibility of the silicon effected the precision of the mould. the bottom sagged under the weight of the SS causing a curved bottom on the specimen.

3.1.6. Discussion on production methods

For the production of specimens during this research the preference was given to silicon moulds because of the ease of working with it and the flexibility in producing new moulds. The casting method will depend on the test specimen shape. If loading holes are needed in the specimen then closed mould injection casting will be used for its smooth surfaces and for being a representative method for real life use cases. When working with specimens without holes the ring mould injection casting will be used. This providing the same benefits as the closed mould injection casting as well as more control on thickness and the option of using steel moulds. The latter is especially useful if you have a fixed test shape to further increase the accuracy of the specimens.

3.2. Steel reinforced resin used

For this research one combination of resin and steel shot is used. By keeping the SRR consistent throughout testing this parameter will not influence testing results between the setups. The resin used for the specimens is a unsaturated polyester combined with a polyurethane 3 component resin consisting of: SMC Daron 8151, lupranat M20R, butanox LP7-IN and accelerator NL49P The product information provided by the supplier can be found here ([45], [8] ,[2],[3]). These compontents are mixed according to the following weight percentages: 100, 25, 1, 1. The resin has a pot life of 1 hour, giving more than enough time to process the resin.

The properties of the Daron mixture with lupranat B25 instead of M20R can be found in table 3.2.

The difference in the two variants of Lupranat on the strength parameters is expected to be insignificant, so these values can be used. The peak temperature and glass transition temperature in the mixture with SS are significantly lower than without SS. This is caused by the high mass of SS extracting heat from the exothermic reaction. This could influence the glass transition temperature. During testing it is not expected to reach these temperatures. Therefore no problems are expected to arise during this research, but this effect of the glass transition temperature is still being researched.

	$E[GPa]$	$\sigma_{max}[Mpa]$	$\mu[mPa.s]$	$T_g[^\circ C]$	f_c	f_f	ν	$T_{peak}[^\circ C]$
Daron 8151/B25	3.3	95	150-220	135	-	-	-	220-260
Daron 8151/B25 + SS	16.2	-	-	-	74.3	10.1	0.13	32.3

Table 3.2: Known material parameters of Daron 8151/B25 provided by AOC and Daron 8151/B25 in combination with SS found in research ([14],[11]) and tests done by A. Christoforidou and R. Verleg

The resin is measured by weight and mixed with a stir bar using figure 8 movement. According to the manufacturer this reduces the air inclusion during stirring. After mixing it is left to rest for 10 minutes to give large air voids time to escape. afterwards it is gently poured in the moulds or syringes to prevent new air voids to arise.

The SS used for the production is steel shot S330/1mm with a weight fraction of 80% SS to resin. It is assumed that the SS will arrange in the optimum packing.

3.3. Specimen shapes

During the production and testing of CT and SCB specimens some problems with the standard shape became apparent. To improve the testing modified shapes where chosen. To start of, the interlocking of the SS made filling the corners of standard CT specimens with SS impossible. For this reason preference went to 2TCT specimens where the tapering prevented the SS from interlocking. The problems of global instability and failure of loading holes were found not to be an issue because the applied forces were rather low. The notch in the 2TCT specimen was designed in the regular way, where the crack tip is usually made with a razor blade. However this was not possible with the SRR, resulting in a blunt initial crack tip. Two alternative methods were developed for the SCB specimens. First a sharp V shaped notched could be made in the specimen. By making a wider base for the notch the mould could end in a sharper tip. Another method would be installing a thin sheet where the notch would be and including this in the cast. The sheet would need to prevent the resin from binding and not form a strong bond with the resin. This, again, would lead to a sharp crack tip. The first method relies on a sharp mould. Depending on the negative used to produce the mould and the mould conditions this sharpness might vary. The specimens produced with this mould will have constant notches. The sheet induced tip can vary a lot between the casts because it has to be applied every cast and can't be reused. It will also be prone to bending and folding leaving the specimen unusable. This can be prevented by carefully filling the mould or using a more stable sheet shape.

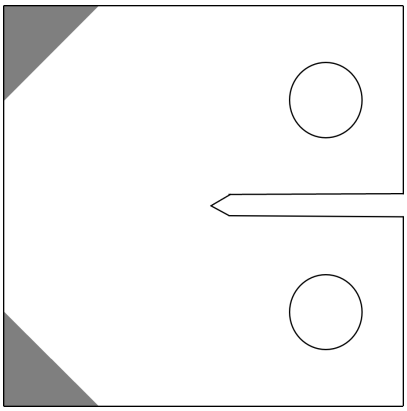

(a) Standard CT specimen gray areas indicating problematic areas

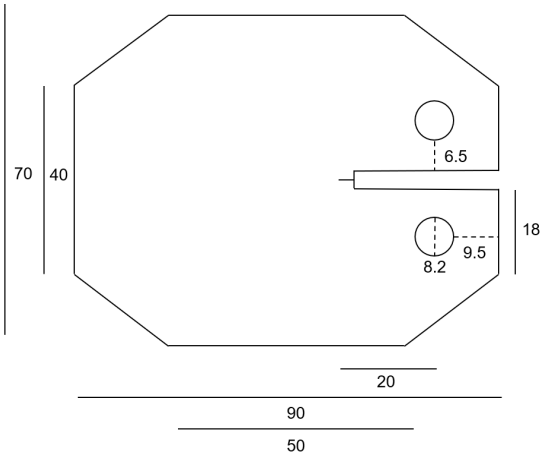

(b) TNB design dimensions t = 20 mm

Figure 3.2: design dimensions 2TCT fatigue testing in mm

The production of the SCB specimen gave one major issue: the arch caused the ideal casting hole to be exactly at the loading point. The large irregularities in the specimens at the casting hole caused problems of stress concentration, crushing of material and turning of the load pin. To work around this the casting holes needed to be moved. But moving them lower than the highest point of the arch made it impossible to fill the complete arch with SS. Moving the casting hole to the bottom of the specimen would lead to the same problem as with the regular CT specimen. Together with this regular SCB relies on a sawed notch that to produce a sharp notch. Because of casting difficulty and the problem with the notch a new shape was designed to still perform 3 point bending tests. In this new shape, the large height of the SCB specimen needed to be preserved. The sharp wider notch was used. The better workability of this solution was preferred over the sharpest option, a thin sheet notch. The top was flattened to make room for two casting holes and still have a smooth loading point. Lastly the corners had an angle of only 45° to prevent the interlocking of SS, leading to sides without SS and to improve the global stability. See figure for the final tapered notched beam (TNB) specimen 3.3. Lastly the thickness of the specimens was increased. By increasing the thickness the effect a possible air void will have on the crack propagation path will be reduce. It will also increase the global stability of the specimen.

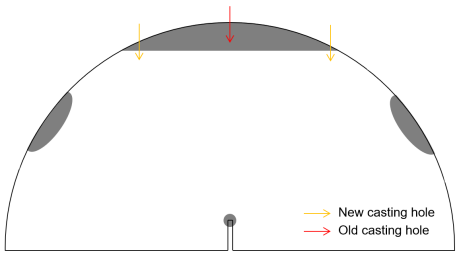

(a) Standard SCB specimen, gray areas indicating problematic areas

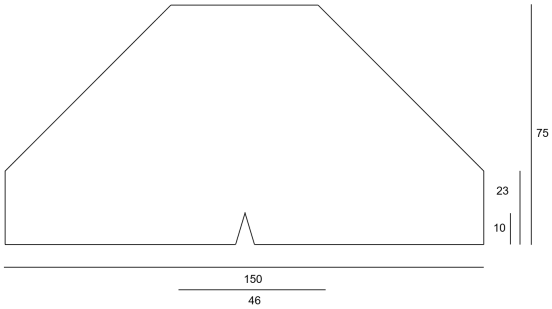

(b) STNB design dimensions t = 20 mm

Figure 3.3: design dimensions specimens fatigue testing in mm

3.4. 2TCT test specimens

The 2TCT specimens are produced using closed mould injection casting. The mould was made using an FRP negative. During production some specimens showed noteworthy visual marks on the surface. To clearly indicate these marks figure 3.4 shows a clear specimen. Large differences between the surface smoothness were found between the specimens. On some specimens the RSS did not completely

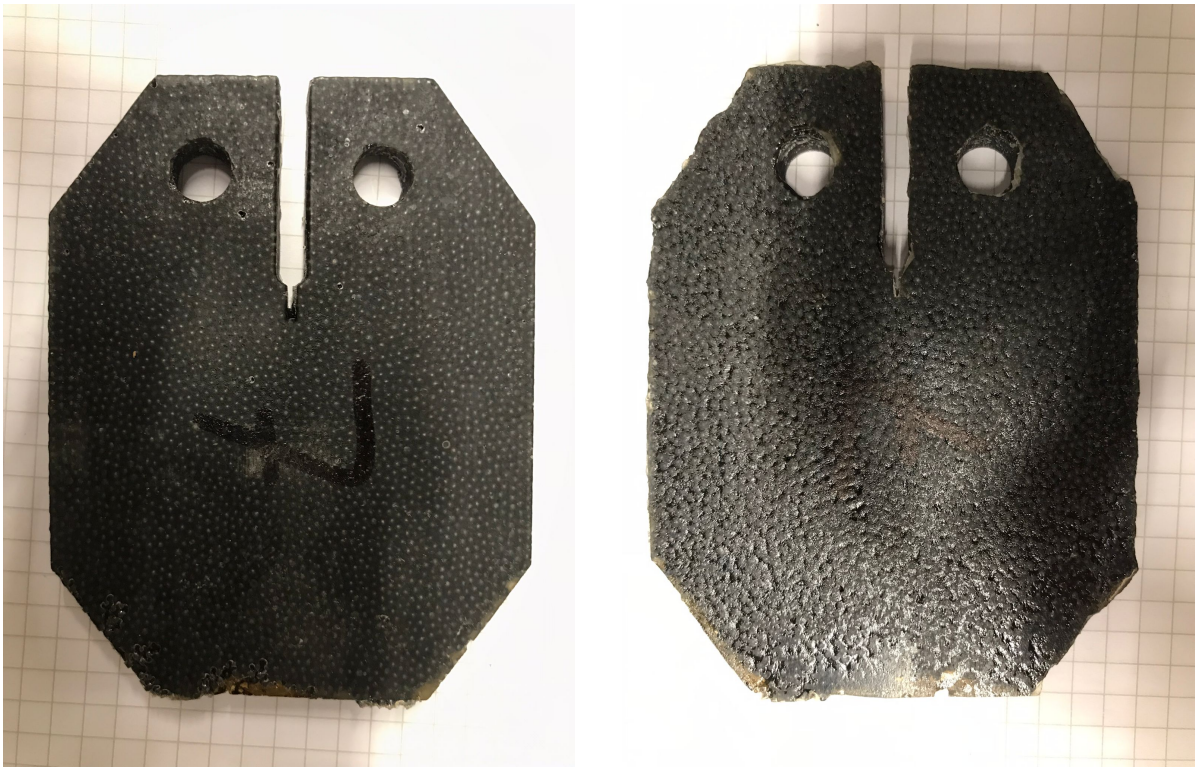

(a) 2TCT specimen 7 front

(b) 2TCT specimen 7 back

Figure 3.4: Example of clear 2TCT specimen

fill all the voids on the surface. This flaw will be referred to as Surface Imperfections (SI), figure 3.5a. The production method left the possibility of steel shot shortage, resin shortage or both at the right edge of the specimens. These flaws will be referred to as Steel Shot Shortage (SSS), Resin Shorage (RS) and Total Shortage (SH), figure 3.5b,3.5c,3.5d. The last flaw found in some specimens was a small amount of rust. The cause of this was unclear but it was assumed that the rust would have no further effect on the specimen and thus it will not be referenced further. Initially the cover plates used for the production where polyurethane plates. The polyurethane showed a reaction to the acetone used for cleaning of the plates. This made proper removing of resin on the plates impossible. For this reason the switch was made to glass cover plates. With this switch the visual marks found in the specimens was greatly reduced. Indicating that the low chemical resistance of the polyurethane was resulting in imperfections.

Due to measurement error specimen 2 had 10x more Butanox and NL-49P than intended. This specimen was meant to be removed from testing but unexpected failure of other specimens resulted in a shortage of specimens, so the specimen was eventually used but only as an indicator test on the testing method.

The dimensions of the specimens showed an average standard deviations of 0.34 mm between the different specimens. However the thickness and the weight of the specimens showed a larger deviation: the standard deviation was 4.29% and 4.41% respectively of the average values. This was caused by filling the moulds with the maximum amount of steel shot in each first filling, rather than measuring the SS before pouring. As the SS is accountable for most of the weight or SS by far, this led to large differences in weight between the specimens. The thickness was also influenced by the first filling and the force applied by the clamps. The dimensions and weight of all the 2TCT specimens can be found in appendix A.

3.5. TNB test specimens

The TNB specimens were produced using the ring mould injection casting. The mould was made with a wooden negative. The dimensions of this negative where slightly off from the design dimensions. The

(a) surface imperfections 2TCT 11

(b) Steel shot shortage 2TCT 12

(c) Resin shortage 2TCT 6 after failure

(d) Total shortage 2TCT 1

Figure 3.5: Visual imperfections in closed moult casting

Specimen name	Visual marks	Test marks
2TCT-1	Open mould casting	Static testing
2TCT-2	10x more Butanox and NL49-P, Crack region SI, SR (polystyrene cover plate)	Displacement controlled testing
2TCT-5	SR, Top and crack region SI (polystyrene cover plate)	Failure during pre-loading
2TCT-6	SSS, notch tip SI (polystyrene cover plate)	Static testing
2TCT-7	Clear (polystyrene cover plate)	Force controlled testing
2TCT-8	Crack region SI (polystyrene cover plate)	Force controlled testing
2TCT-9	SSS, Back SI (polystyrene cover plate)	Displacement controlled testing
2TCT-10	Top SR and SI, back SSS (polystyrene cover plate)	Failed test
2TCT-11	Crack region SI	Increment controlled testing
2TCT-12	SSS	Increment controlled testing
2TCT-13	SSS	Increment controlled testing
2TCT-14	SSS	Increment controlled testing
2TCT-15	SSS	Increment controlled testing

Table 3.3: Notes on the 2TCT specimens

notch was 7.5 mm high instead of the intended 10 mm. The notch was also not as sharp as designed because of the saw lines in the wooden negative. The same visual indicated imperfections as found in the 2TCT specimens are possible in the TNB, see table 3.4.

Specimen name	Visual marks	Test marks
SCB-1	Open mould casting	
TNB-1	SSS	
TNB-2	SSS	
TNB-3	SSS	
TNB-4	Sheet induced notch	

Table 3.4: Notes on the TNB specimens

The dimensions of the specimens showed an average standard deviations of 0.87 mm between the different specimens. However the height of the specimens showed a larger deviation: the standard deviation was 2.32% of the average values. The main reason for this is the sagging of the ring mould under the weight of the SS. The larger thickness increased the weight on the mould. The mould also needed to be higher and is thus more flexible. This led to the sagging of the bottom part of the mould, leading to a curved bottom of the TNB specimen and high deviation of specimen heights. To TNB specimen 4 a sheet induced notch was added to counteract the blunt notch found in specimen 1,2 and 3. For this purpose a piece of resin repelling paper was folded and added to the mould to introduce a sharp notch. The paper was removed after casting. The result was a sharp, but varying in lenght and width notch from front to back of the specimen. Again, these dimensions can be found in appendix A

(a) Visualization of sheet notch in mould

(b) Front of notch after casting

(c) back of notch after casting

Figure 3.6: Visualizations of paper induced notch

3.6. Discussion on the production of complex shapes with SRR

The chemical resistance of the cover plates and moulds shows a large impact on the visual marks on SRR cast specimens. This became especially apparent when the switch between polystyrene to glass cover plates was made. This signifies the importance of using moulding materials with high chemical resistances when working with SRR. The earlier casting methods show that easier casting methods produce higher inaccuracy's. This illustrates the fine balance between time and resources available and the accuracy required of the test you need to perform. For the hands on approach of testing in this research the flexibility of an easier production method was preferred, even though this led to less accurate results. When working with predefined testing setups where moulds are preferred, high quality silicon moulds could be produced or when no loading holes are needed steel ring mould could be used. To further increase the quality of the produced specimens various techniques can be used to remove air voids from the specimens. Examples of this are using a shaker to remove trapped air, curing the resin in a vacuum chamber or injecting the resin under high pressure. The visual marks that were found on the specimens could be investigated further by looking at the exact forces close to the point of SSS, RS and SH defects. The effect of these surface imperfections can be investigated by testing the air void content of the specimens. This could be used to explain differences between the specimens found during testing.

4

Compact tension testing

In this chapter the different testing methods tried on the doubly tapered compact tensions (2TCT) specimen are reported and discussed. The attempts here gave insight on the behaviour of the material and on the challenges facing when running tests. The different solutions will be discussed and the knowledge will be used in the semi-circle bending testing and further recommendations. In chapter 6 these tests are validated using FEA models. Some early static tests are performed to learn of the static behavior of the test method and find the critical stress intensity of the material. But, the main focus is on the fatigue tests. The first tests were done to be able to achieve a stable crack propagation within a feasible time. Later test are used to define the Paris Law of the SRR.

4.1. Setup

The testing was done on a universal testing machine (UTM-25) with a load range of 25 kN. The clevis and pin used for the loading can be found in figure 4.1. For the DIC pictures a Canon EOS 5Ds with a macro 100mm lens is used. For the static test a ramp function is used to apply the load. The loading in the fatigue test was done with a sine wave with a frequency of 1 Hz on all fatigue tests. The photos were taken after x amount of cycles where the load was increased up to the maximum. The loading was monitored and controlled with the program MP3. Separate scripts were run inside MP3 to control the photo frequency and loading during photo. See figure 4.2a, 4.2b and 4.2c for the setup and the program used to control the loading. After installing a specimen for testing, carefully, a small load was applied to remove any offset of the loading pins. During this process a number of specimens shattered, leading to a lower initial force being applied. This leaves a large chance of an initial off-set. This small initial force was lost in all force controlled tests after the first couple of cycles. The result is a fatigue loading not following a targeted sine wave but resulting in small impacts on the specimen. In those instances the max force is taken as the force range thus R is exactly 0.

4.2. Static test

Two static tests were performed on the 2TCT specimens. The first one was performed on a specimen produced with open mould casting. This one was used together with a open-mould cast semi circular bending (SCB) specimen to indicate the form with the highest potential for stable crack propagation. The latter test was to give an indication of the strength of the 2TCT specimen. The tests were performed with different loading speeds. This made it difficult to compare the influence of the casting method. The decrease of loading speed was done to have more feedback on the crack propagation path. The first static test had an upwards crack path. With the goal to see more clearly the deviation of a strait crack path, the loading speed was decreased. See figure 4.3 for the crack paths of the two static tests.

From static test 1 it can be seen that the specimen has some stiffness left when the first crack was found, see figure 4.4a. The maximum stress intensity can also be found of this method and the expected displacement at failure. However, the switch in production method made it so that this value had to be reconsidered. Therefor the second static test was performed, see figure 4.4b. The displacement at the crack was 0.29 mm with a force of 693.711 N leading to a stress intensity of 39.66 according to

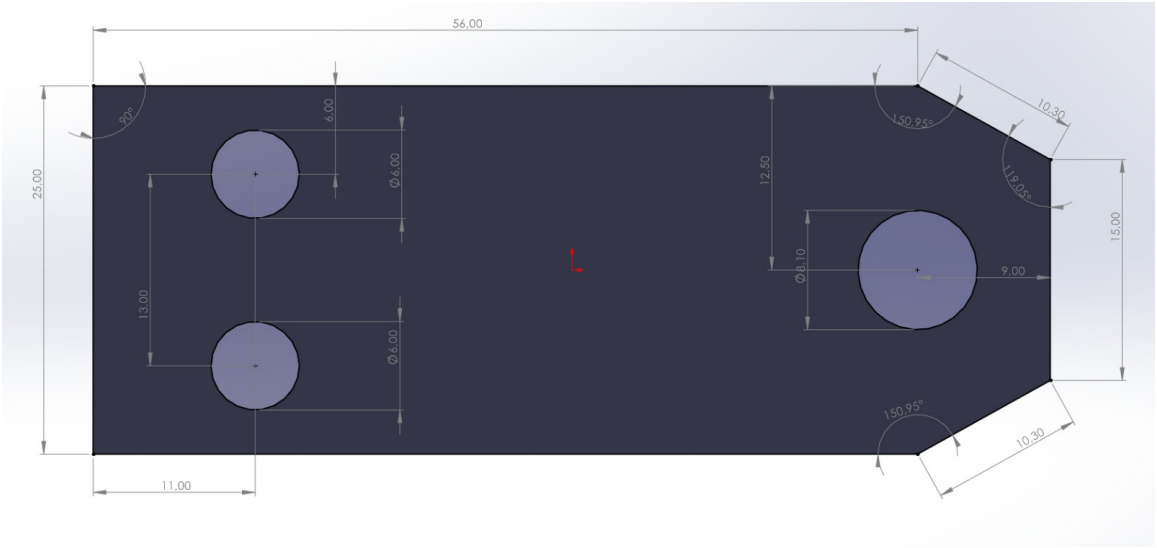

Figure 4.1: Dimensions of clevis in mm

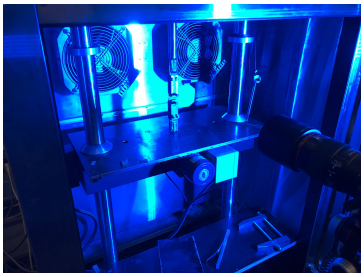

(a) Test setup 2TCT testing

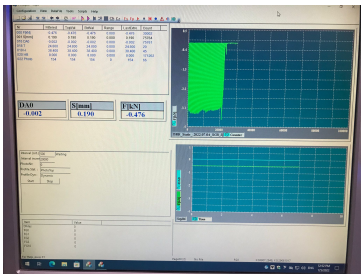

(b) MP3: used to form Force and displacement functions for testing

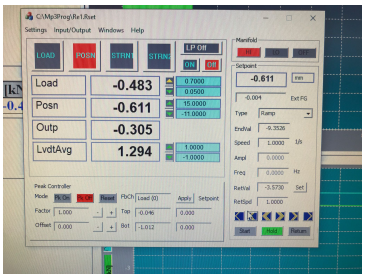

(c) Re1: used to directly link the function control of MP3 to the UTM-25

Figure 4.2: Testing setup 2TCT

equation 2.6. These values were used as an initial estimate for the displacement and force on which the fatigue testing was done.

4.3. Fatigue testing approach

For the fatigue testing a trial and error approach was taken with the goal of achieving stable crack propagation within a feasible time. See figure 4.5 for the step by step approach. Force-controlled/ stress intensity increasing testing will results in the shortest tests. However, this method has the highest chance of unstable crack growth. The force-controlled method would lead to a complete Paris Law plot in one test, but might miss some data around the lower bound. The displacement-controlled, or stress intensity decreasing, testing has a higher chance of stable crack propagation. The drawback is that the unstable crack growth will never be reached and the initial displacement might not be enough to utilize the available crack length. Also in this method the crack would grow less over time, so more cycles are needed before the end of the crack growth is reached. The last method that was initially proposed is constant stress-intensity testing. With this method the stress intensity will be kept constant so a stable crack growth is more or less guaranteed. This does however mean more tests with different stress intensities are required to find the Paris Law of the material. Moreover, this method would be more difficult to perform testing with. This is due to the immediate regulation of the force by direct measurement of the crack length during testing. Thus this would be a last resort if no other methods are promising. During the setup of the testing there were some initial problems that made starting with force control testing impossible so in the interest of time the first tests were done with displacement control during which the problems with force controlled were sorted out.

The first displacement and force values were taken from 30% of the maximum found in the static

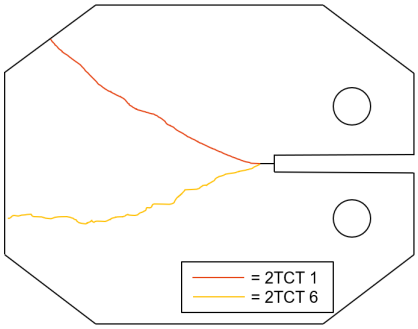

Figure 4.3: Visualisation of the crack paths of the static tests

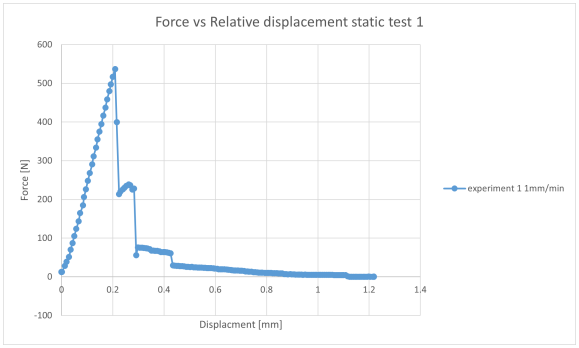

(a) Force vs Displacement of static test on 2TCT 1

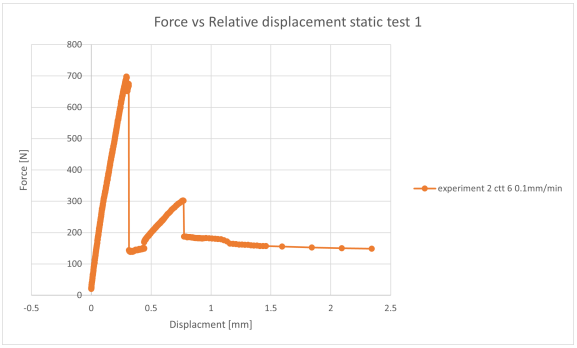

(b) Force vs Displacement of static test on 2TCT 6

Figure 4.4: Results of static 2TCT tests

test. From here, modifications were done with the insight given by earlier tests. In total 9 tests were done on 2TCT specimens. From this 4 of the tests were used to decide on the final method and 5 were repeats with the same method.

The stiffness loss during testing was used to indicate the potential of stable crack growth. The less stiffness was lost in a short time span, the more stable the crack growth should be. Next to this the following was considered:

- The digital image correlation (DIC) images
- The final crack path
- The amount of cycles between crack start and end crack growth

The cycle count between start end end was done by visual indication of the crack on strain plots against the reference stage. Reference stage referring to the stage where no extra loading was applied to the specimen. Because of the computation time needed to find the exact crack length of the tests this was not done when considering the potential of the tests.

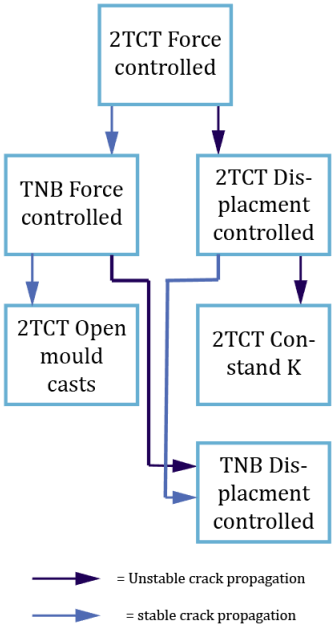

Figure 4.5: Visualisation of intended steps for the fatigue testing

4.4. Crack length determination using digital image correlation

The processing of the images was done using GOM Correlate. The crack length was found using the difference in displacement between a surface curve above the crack and one below the crack. The crack length was taken as the furthest length in y of the surface curve where the distance, against the reference stage, between the curves was bigger than the cut-off limit. With the reference stage being at $N = 0$ and $F = F_{min}$. The cut-off limit was decided by measuring the crack length in one image and finding the distance between the surface curves associated with this length. Two methods for drawing the surface curves were tested: Direct following of the crack path and global following of the crack path. Both curves were drawn close to the crack (<2mm) and away form the crack path ($\pm$ 5mm). The first of a pair of curves was drawn the second was constructed using an offset in y direction. When the distance has a lot of variation in one stage the crack length along the test will show more jumps. The closure the distance is to 0 at the real crack length the more accurate the crack length can be detriment. However, the cutoff limit gives some freedom to work around this problem. Because of the freedom with the cutoff limit the deciding factor is the amount of variation in the distance plot. In figure 4.7 it is clear that the away global following surface curves show the least amount of spikes. All the surface curves result to almost the same distance between the curves at the measured crack length. Because of this the global following of the surface curve is used to determine the crack length during experiment.

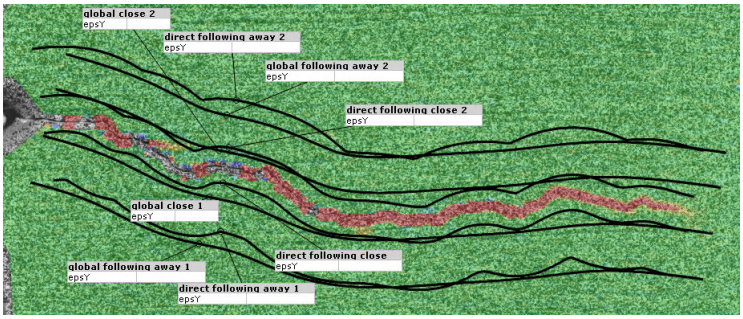

Figure 4.6: Visualization of surface curves locations and methods

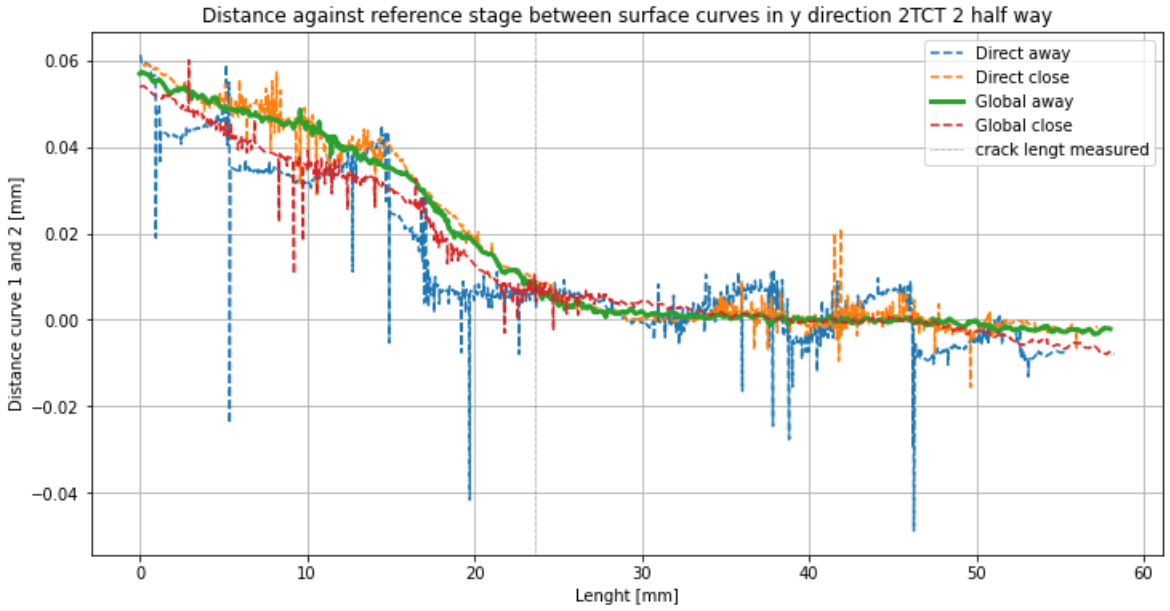

Figure 4.7: Effect of surface curve on the measured distance

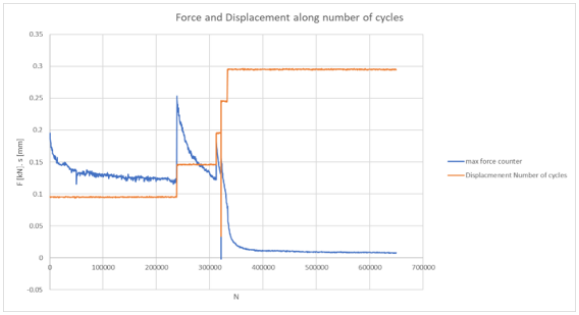

(a) Force and displacement vs cycles 2TCT-2

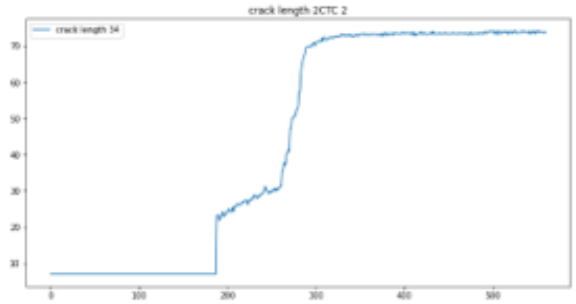

(b) Crack length cut-off limit = 0.01 mm

Figure 4.8: Results 2TCT-2 displacement controlled fatigue test

4.5. Results

First the results of the 4 trail test will be shown and the decisions based on those test will be explained. Then the final method will be discussed and the results of those tests presented.

4.5.1. Displacement controlled 2TCT-2

The test started with maximum displacement of 0.1 mm and minimum displacement of 0.02 mm. During the test it became apparent that the specimens lost a lot of stiffness without any visual crack growth. After the first 200000 cycles no indication of crack forming was found. Because of the desire to see at which displacement the crack would start to grow, the maximum displacement was increased after 237445 cycles. This was done again at 312068, 321162 and 333082 cycles. The displacements were respectively 0.15 mm, 0.2 mm, 0.25 mm and 0.3 mm. After the last increase it was left to run till 649570 cycles to see if the crack would stop growing. The processed results showed that the crack did initiate after the first displacement increase, in contrary to what observations with the naked eye showed. After crack initiation the crack had a steady growth but the maximum 0.03 mm difference between the surfaces curves gave deviating results. During the following displacement increases no really stable crack growth rate could be indicated because it followed rather quickly. Looking at the crack path it is clear that the crack tip deflection and meandering plays a large roll in the crack growth. Furthermore some crack branching can be found in the specimen. Because a rather stable stiffness loss and crack growth was found, follow up tests was done using force control.

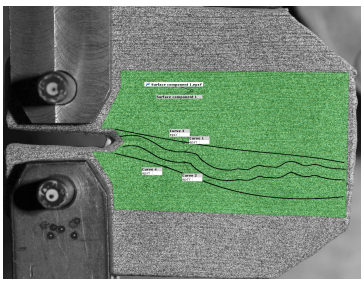

(a) Crack after first loading

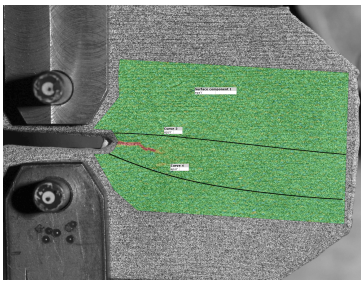

(b) Start crack N = 238000

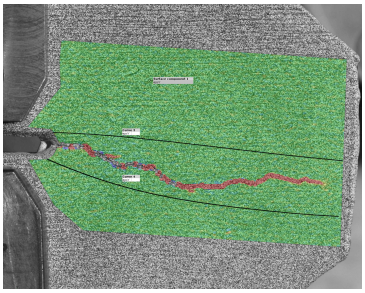

(c) Final crack N = 649000

Figure 4.9: Crack path 2TCT 2

4.5.2. Force controlled 2TCT-7

The first force controlled test was started with a maximum force of 0.25 kN, approximately the same as the force at crack initiation of the 2TCT-2 test, and a minimum of 0.02 kN. R = 0.08. The test was left to run for 523247 cycles in this force range. No crack growth or increase in displacement range was found during the 500000 cycles. The force was then increased to a maximum of 0.35 kN, R = 0.05. The result was failure in 20397 cycles. With only 7000 cycles between initiation of crack and failure this was indicated as a unstable crack growth. The crack deviation from a strait crack path was significant in this test. The misalignment of the loading pins was the cause of this deviation. Because of this it was decided to try a second force controlled test to see if the deviation impacted the crack growth.

4.5.3. Force controlled 2TCT-8

The second force controlled test was started with a maximum force of 0.30 kN and minimum force of 0.02 kN. R = 0.067. No final crack path can be found with the DIC because of the total failure of the specimen. The crack path started out 'straight' and the final failure is also straight. Even though the crack path did not deviate it still failed withing 8000 cycles from initiation of the crack. Together with the large jump in crack length between the last 500 cycles the stabler crack growth in the displacement controlled tests was preferred.

4.5.4. Displacement controlled 2TCT-9

Maximum displacement was 0.25mm and minimum 0.02. In this test it did result in a really small negative bottom force. Over time the loading pin moved and fell out of the specimen. However the crack growth was already negligible at this point. The maximum displacement lead to large sudden crack before fatigue loading started to effect the crack. After 40000 cycles the maximum crack length was almost already reached. So the next 760000 cycles nothing really happened.

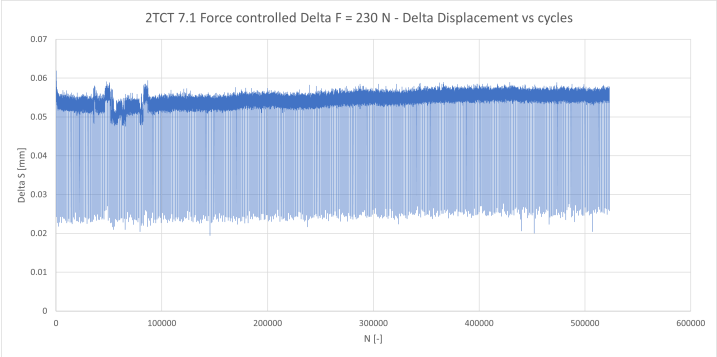

(a) 2TCT 7.1 - Delta displacement vs cycles R = 0.08

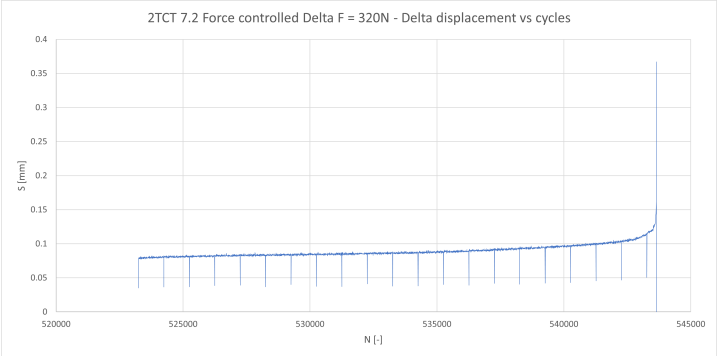

(b) 2TCT 7.2 - Delta displacement vs cycles R = 0.05

Figure 4.10: Results 2TCT-7 force controlled fatigue test

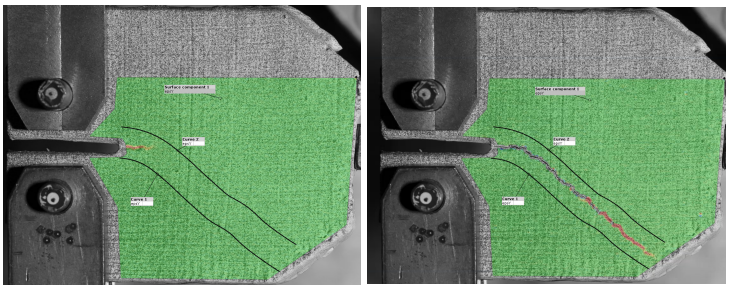

(a) Start crack N = 536500 (b) Final crack N = 543500

Figure 4.11: Crack path 2TCT 7.2

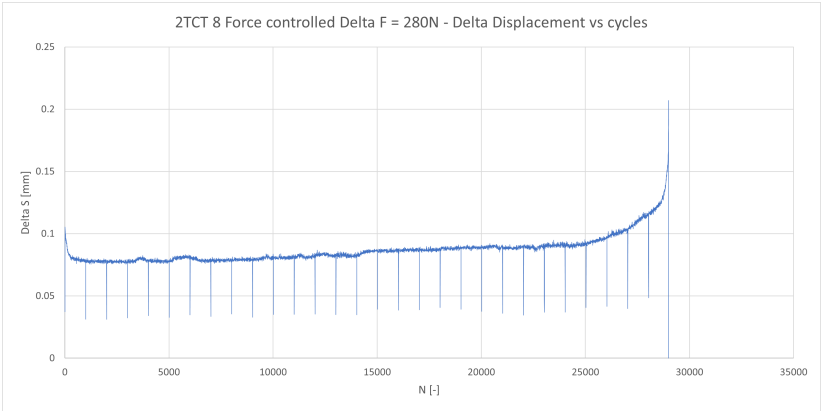

Figure 4.12: 2TCT 8 - Delta displacement vs cycles R = 0.067

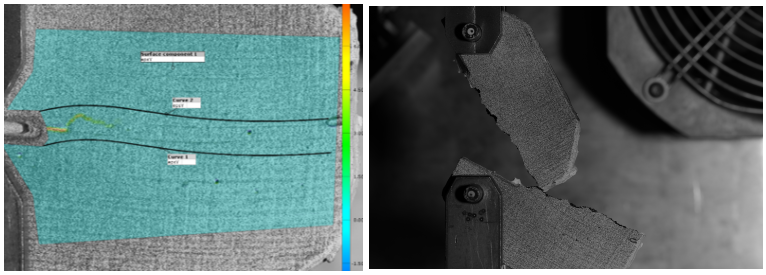

(a) Last measured crack DIC N = 28500 (b) Final crack N = 28999

Figure 4.13: Crack path 2TCT 8

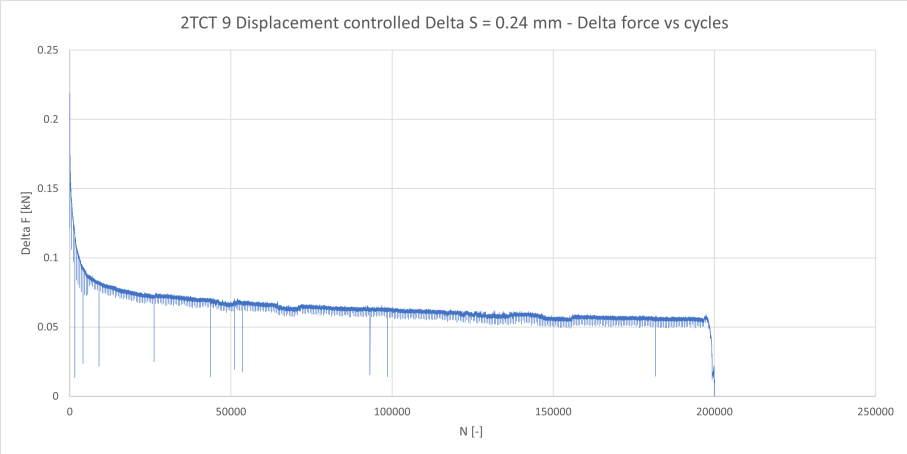

Figure 4.14: 2TCT 9 - Delta force vs cycles R = 0.1

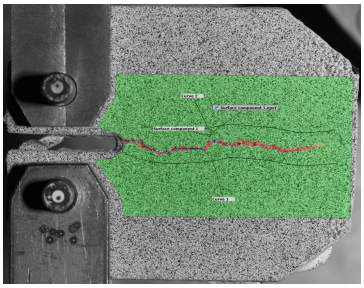

(a) Crack after first loading

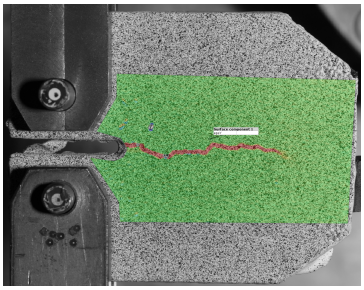

(b) Crack 40000 cycles

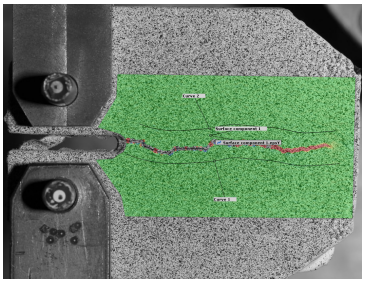

(c) Final crack N = 800000

Figure 4.15: Crack paths 2TCT 9

4.5.5. Displacement controlled increment testing results

Because of the risk of removing the crack pin, the testing machine was set to not allow any negative forces for the following tests. During the trial testing, it became apparent that the displacement or force needed to initiate the crack varied between the specimens. Another thing was that the displacement controlled tests ran for long time. To improve on both points, increment testing was applied as a final method. The increments were set to 40000 cycles increasing the maximum displacement from 0.20 mm up to 0.35 mm with steps of 0.05 mm. The minimum displacement was increased from the trail runs from 0.02 to 0.05 mm in an attempt to keep force on the specimens. However even with the increased minimum displacement, the minimum force became smaller than 0.005 kN after 500 cycles for all 5 tests. Resulting in a R-value of approximately 0 and the use of the maximum force and stress intensity instead of the range.

Working with one cutoff limit to determine the crack length for the specimens did over- or underestimate the crack length, depending on where the cutoff limit was taken. With overestimation at large crack length when the cutoff limit was taken at small crack length and underestimation at small crack length when the cutoff limit was taken at large crack length. In the increment testing the displacement in y gets increased along the testing. Resulting in large increase of the difference between the two surface curves. To counteract the over- or underestimation two cutoff limits were found for every test. The first was for the first 2 increments and taken at the crack start. The second cutoff limit was used for increments 3 and 4 and taken at the crack after 40500 cycles. The GOM software had a minimum measurement steps 0.001 mm difference between the two curves. Within the small displacement of the testing the crack length was found to be sometime within this step. In these instances the crack length can vary up and down resulting in theoretical negative crack growth. Because this should not be possible as the material does not have any self healing properties these negative crack growths are removed from any Paris plots. The test on 2TCT 12 showed crack initiation at the middle of specimen. This could be caused by large air voids around this point or pollution in the resin, resulting in large stress concentrations and crack initiation from this point. Especially when the crack tip is not sharp, the voids or pollution's can cause higher stress intensity. The first increment of every test shows high difference in crack length between the specimens and in most of the tests minimum crack growth. This means that the fuzz on the found date has large effect on the results together with the initiation of the crack not being part of the Paris curve, this led to disregarding of this part of the test. The last increment also shows really low crack propagation. Small errors in the data will cause large scatter in the Paris plot, thus the last increment is also disregarded.

	2TCT 11	2TCT 12	2TCT 13	2TCT 14	2TCT 15
cut-off 1	-0.005	0.005	-0.014	-0.015	-0.007
cut-off 2	-0.008	0.011	-0.017	-0.02	-0.007

Table 4.1: Cutoff limit used to determine crack length, + or - depending if the distance between top and bottom or bottom and top surface curve is used

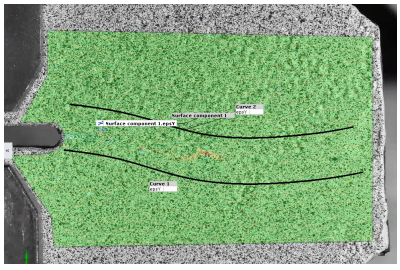

Figure 4.16: Crack initiation in middle of 2TCT 12

Using the crack lengths and equation 2.6 the Paris plot can be constructed. Special care is taken to remove the data when an increment increase takes place. This would create points with high da/dN that is not due to fatigue loading. The da/dN is found between two points separated by an amount of cycles equal to the step size. The K is calculated using the average crack length and average force between the two points. Data with a negative or zero crack growth are removed from the plot. By

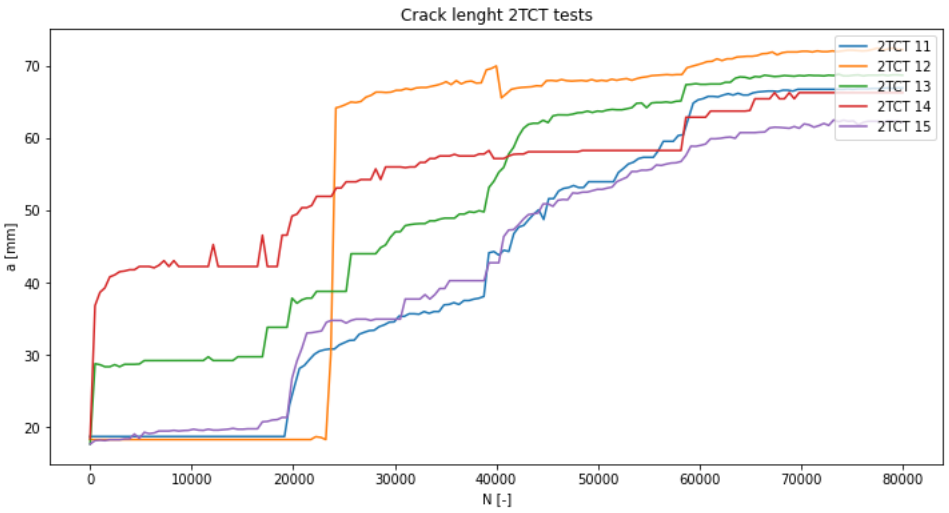

Figure 4.17: Crack lengths 5 2TCT incremental increased displacement control testing

increasing the step size the amount of data points are reduced, losing some data, but outliers due to local fuzz on the data are subsequently removed. The resulting Paris plots show a large scattering of points. Even when the step size is increased to 5000 it still has a large scattering. From this data no clear Paris Law can be found.

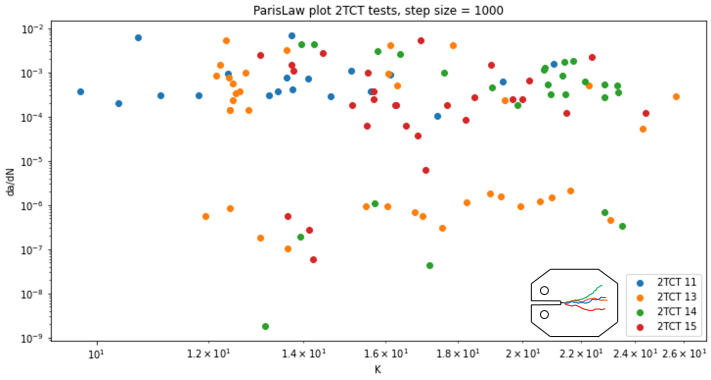

(a) Paris plot, step size = 1000, increment 2 and 3 of specimen 11,13,14 and 15

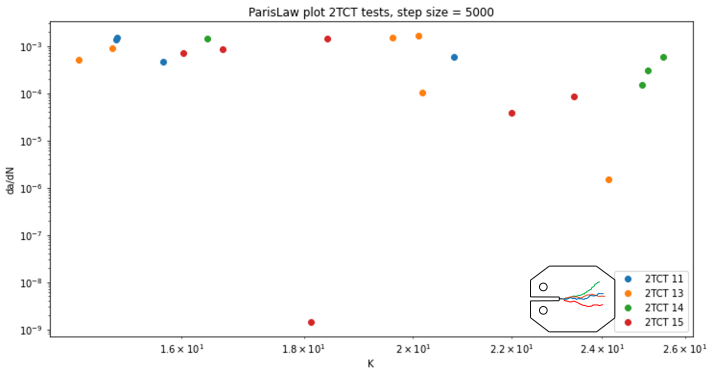

(b) Paris plot, step size = 5000, increment 2 and 3 of specimen 11,13,14 and 15

Figure 4.18: Paris plots and effect of step size on scattering showing final crack paths

To further reduce the noise of the data, the Paris plot can be constructed from curves fitted to plots of the gathered data. Up to a sixth order polynomial and log formulas were fitted using non-linear least squares to fit the function for crack length vs number of cycles, and force vs number of cycles data. To

compare the accuracy of the fitted function the standard error of the regression (S) and R-squared is used. Using fitted curves will remove any outlier and fuzz, but by doing this the data will be simplified a lot. The real life The stiffness loss during testing was used to indicate the potential of stable crack growth will be lost on the uses of any found Paris Law. From this fitting the quadratic function shows the best fit according to the S with an average S of 2.34 and 0.031 for the a-N and F-N plots respectively. However, the R-squared value showed a high jump in the polynomial functions to values far below zero. Because of this the log function was used to construct the Paris law data. The exact differential of the a-N curve together with the force is used to plot the Paris plot. By removing the averaged values from the equation, the plots show no clear linear correlation.

function		log	2e	3th	4th	5th	6th
a-N	Standard error of regression	5.97	2.32	10.39	61.57	460.5	3.517e3
	R-squared	0.85	-718.6	-1.29e4	-1.14e6	-3.178e9	-1.36E+12
F-N	Standard error of regression	0.081	0.031	0.064	0.25	1.42	9.934010146
	R-squared	0.91	-735.1	-1.37e5	-1.29e7	-5.36e8	-2.09e10

Table 4.2: average S and R-squared for 2TCT 11,12,13,14 and 15 curve fitting

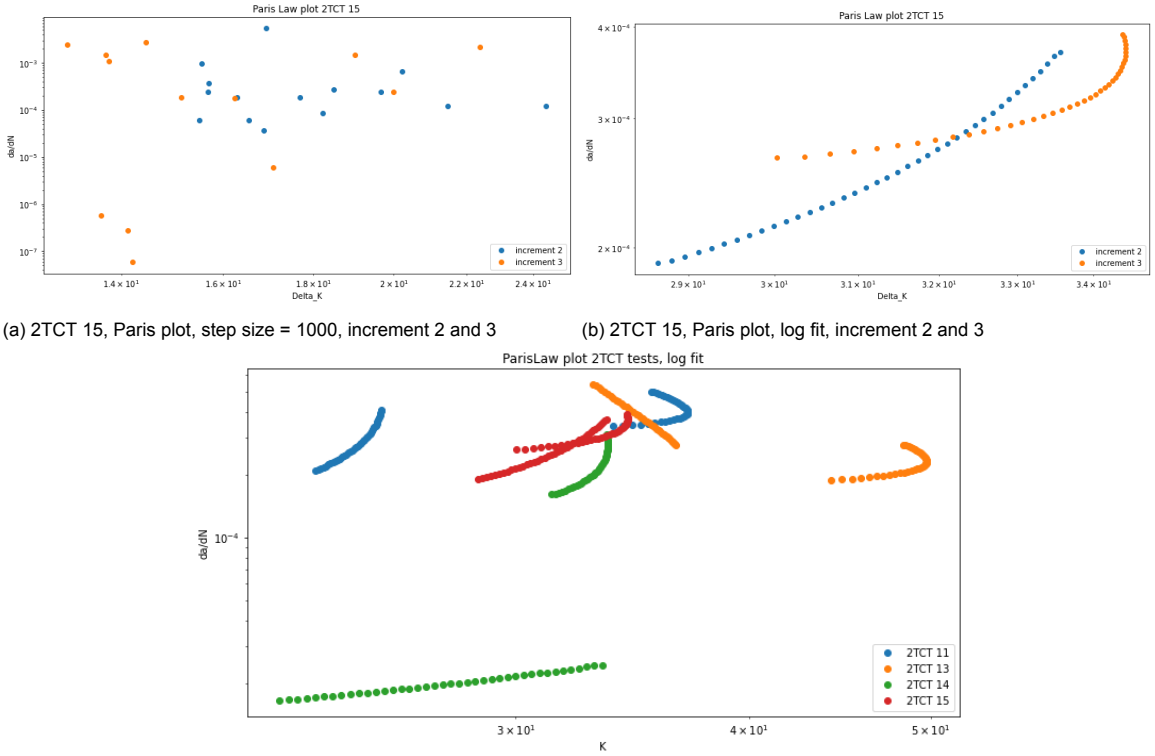

(a) 2TCT 15, Paris plot, step size = 1000, increment 2 and 3

(b) 2TCT 15, Paris plot, log fit, increment 2 and 3

(c) Paris plot, log fit, increment 2 and 3 of specimen 11,13,14 and 15

Figure 4.19: Paris law log fitted 2TCT 15 and all specimens

4.6. Discussion

The compact tension test achieved the desired stable crack growth within displacement control tests. The displacement control did however lead to long testing time, especially with the low frequency used. For the low frequency displacement controlled tests, incremental maximum displacement shows to be promising to reduce testing time, while still using the complete possible crack length. Working with smaller specimens with only one increment and more specimens would also be an option to reducing testing time and still making optimal use of materials. With the added risk of complete failure of specimens in the first displacement wave. Using 2TCT specimens with displacement controlled testing the Paris plots show no linear correlation and a large scatter of data. The large scatter of the data could result from the many deflections of the crack tip during crack growth in the material. It could also be that voids in the material influence the crack growth. Another explanation might be that the small forces and displacement result in noisy data for the found forces and especially in the crack length. This can already been seen by the high S value when trying to fit different functions to the a-N data points. Trying to reduce this scatter by using curve fitted functions representing the data has mixed results. The scattering is reduced and some overlay of the data can be found, but still no clear linear function is visible and some plots suggest unreasonable behaviour. Another peculiar point is that between the different increments of a specimen no real correlation could be found. Off course this could be because of the noisy data. Other reasons for this could be the strain rate depending stiffness of the resin, where between the different displacements the strain rate per cycle changed the behaviour of the specimen. Another reason for this could be the increase in crack length at the increased displacement resulting in chance in extrinsic mechanisms affecting the crack growth.

For now however the main takeaways are that low forces make testing more difficult, the results become more noisy and voids can take up large part of the specimen with thin specimens. For these reasons the 3 point bending tests are of interest over thicker 2TCT because higher forces are found in the TNB form. The TNB were designed with a higher thickness. It is expected that through thickness non strait cracking will increase when working with thicker specimens.

5

3 point bending test result

In this chapter, the testing performed under 3 point bending is discussed. First, the initial static test will be briefly presented. But the main focus is on fatigue testing. The found testing method in chapter 4 is applied on 1 semi circular bending (SCB) specimen and 3 short tapered notched beam (STNB) specimens presented in chapter 3. The effects of the modifications applied to the specimen after the compact tension test and the use of 3 point bending testing for crack propagation testing will be discussed. In chapter 6 the results will be validated using numerical models. The STNB specimen will use the same dimensionless form factor formula as the SCB specimen 2.11. Chapter 6 will try to validate this form factor formula.

5.1. Setup

For the main setup see chapter 4.1. The only modifications to this setup are in the loading method. The loading is applied using a curved surface to apply as close to a line load as possible on the specimens. The same hold for the supports. see figure 5.1 for the test setup and support used.

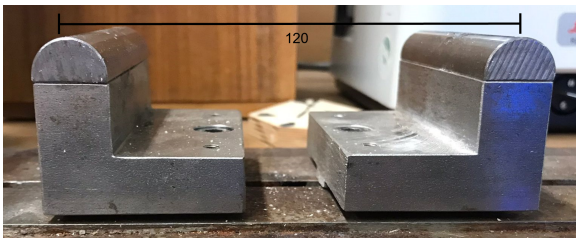

(a) Distance supports 3 point bending test in mm

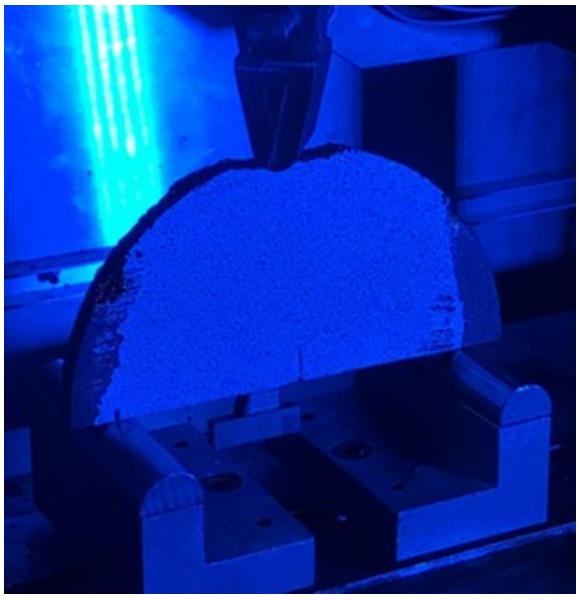

(b) Test setup 3 point bending test SCB-2 rotated loading pin due to uneven top surface

Figure 5.1: test setup 3 point bending

5.2. Static test

An open cast semi circular bending (SCB) specimen was used for the static test. This test was performed together with the static 2TCT test to indicate the crack path and the most promising testing setup. The specimen was loaded at a rate of 1mm/min. The maximum force was 2.44 kN at a displacement of 0.35 mm. The found maximum force is about 3.5 times higher than in the 2TCT specimens while the thickness is only 1.5 times higher. With the static test, no residual strength was left after failure and a brittle failure was found. The brittle failure was the reason that the initial 2TCT test setup was preferred over the SCB. However, after the 2TCT testing, stable crack growth was not the main problem. The low force and displacement in the 2TCT did prove some difficulty. The SCB test performed better on these factors. This is way 3 point bending fatigue tests were done after the compact tension tests.

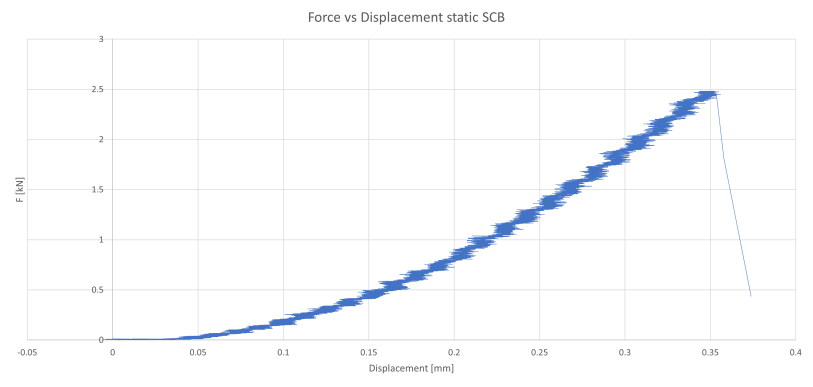

Figure 5.2: SCB-1 static test, force vs displacement, 1mm/min

5.3. Fatigue test

The same incremental increasing displacement controlled test as in the final 2TCT tests was used for the fatigue testing. Here the same relative to the maximum static displacement was used for the first increment with increases of 0.05 mm every increment. The first fatigue test was performed on close mould injection casted SCB specimen 2. However, the casting method led to problems during testing as discussed in chapter 3.5. After this, the STNB specimens discussed in chapter 3.5 were used. Due to time onstraints on the lab equipment, only 4 3 point bending tests could be performed.

	S_max1 [mm]	S_max4 [mm]	S_inc [mm]	F_ini [N]
SCB-2	0.2	0.4	0.05	25
STNB-2	0.35	0.5	0.05	65
STNB-3	0.375	0.45	0.025	400.85
STNB-4	0.375	0.45	0.025	420.66

Table 5.1: Testing values 3 point bending tests

The fatigue test done on specimen SCB-2 started with a maximum 0.20 mm displacement increasing to 0.35 mm with increments of 0.05 mm., the minimum displacement was 0.02 mm. The crack growth rate started in increment 2 and ended in increment 3. The force did however still increase in increment 4. This is due to the better compression performance of the material. Combined with the compression forces in the arch. The specimen was initially loaded with 25N. The initial loading was lost after the first cycles and the minimum displacement resulted in a minimum force of 0. In increment 1 the forces increased. At this point the loading pin started to rotate. The problems with the casting and rotation of the load pin led to the use and design of the STNB for the following fatigue tests. For a more in-depth look see chapter 3.5.

For the fatigue test on specimen STNB 2, the maximum displacement started at 0.35 mm increasing to 0.5 mm with increments of 0.05 mm, minimum displacement was 0.2 mm. The initial loading was increased to 65N. This initial load was again lost after the first couple of cycles. Again no complete sine is found in the loading wave Because of the much higher maximum force on this specimen dimensions

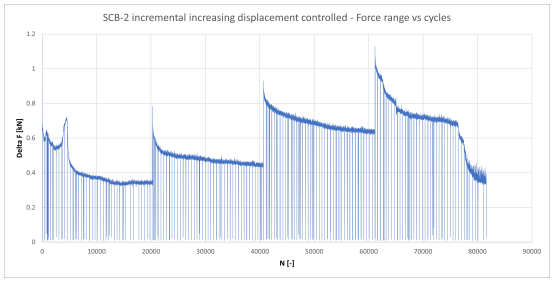

Figure 5.3: SCB-2 incremental increasing displacement controlled, force range vs cycles R = 1

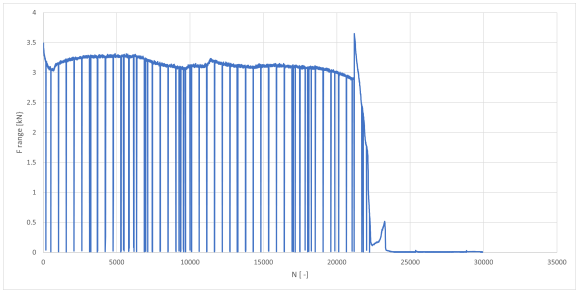

(a) TNB-2 incremental increasing displacement controlled, Force range vs cycles, R = 0

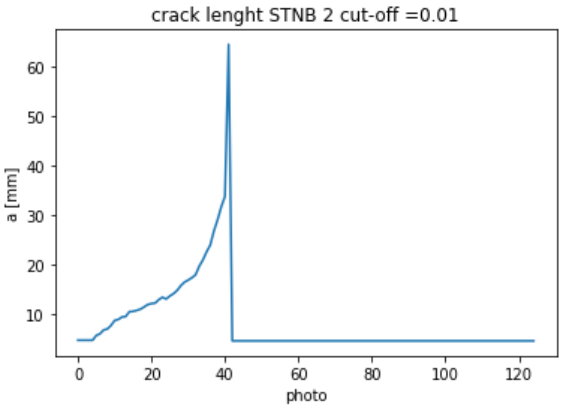

(b) crack length STNB-2, photo was taken every 500 cycles, shattering of the specimen resulted in no measured crack length after photo 41

Figure 5.4: Results fatigue tests STNB-2

the initial force for the following tests was increased even more. The result of the fatigue test where small crack growth in the first increment followed by an unstable crack growth at the start of the second increment. Because of the unstable crack growth, the increment increase was reduced for the following tests. This was to achieve longer stable crack growth, as in increment 1. Because of the higher displacement, only one cutoff was needed to find the crack length in these tests.

For the fatigue test on specimen STNB 3 the maximum displacement started at 0.375 mm increasing to 0.45 mm with increments of 0.025 mm, minimum displacement was increased to 0.5 mm. The initial loading was increased to 400.85N. Both of the increases on the minimum displacement and initial force were to keep the loading constant on the specimen. For the first increment, this was successful. But after the first maximum increase, the force at minimum displacement was zero again. The crack growth started in the second increment so R is still 0. Again the crack growth starts to accelerate in the specimen.

For the fatigue test on specimen STNB 4 the maximum displacement started at 0.375 mm increasing to 0.45 mm with increments of 0.025 mm, minimum displacement was increased to 0.5 mm. The initial loading was 420.66 N. which was lost after about 500 cycles. Resulting in a R of 0. The crack growth and stiffness loss in this specimen is a lot more regular and shows more in common with the expected behaviour in reducing K tests.

The results from the STNB specimens are used to plot Paris curves. Because of the total failure before the final increment only the increments with crack growth are plotted. So, for STNB-2 only increment 1 is plotted, STNB-3 increments 2 and 3 are plotted. For STNB-4 increments 1,2 and 3 are plotted. increment 4 is disregarded because the crack growth will be really small at this point. The method is the same as in chapter 4.4.5, except for the form factor. In STNB-2 the outlier is data from the start of the crack. The start of the crack length as shown in figure 5.4b had a really small crack growth. This is almost equal to 0 and finds place in stage-I of the crack. Thus this point can be discarded from the data. The outlier in STNB-3 is from the last data point. In figure 5.5b it is clear that no crack growth is found after cycle 56000. However, a da/dN slightly larger than 0 is still found. This data point is also discarded. The resulting plot can be found in figure 5.7. STNB-2 and increment STNB-3 both show a

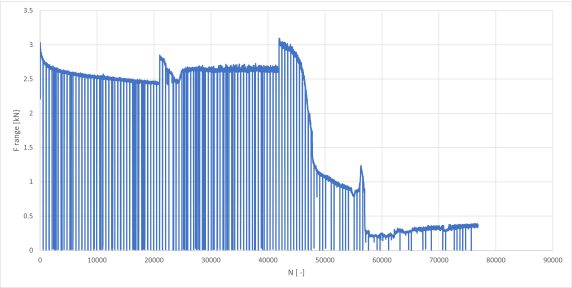

(a) TNB-3 incremental increasing displacement controlled, Force range vs cycles, R = 0

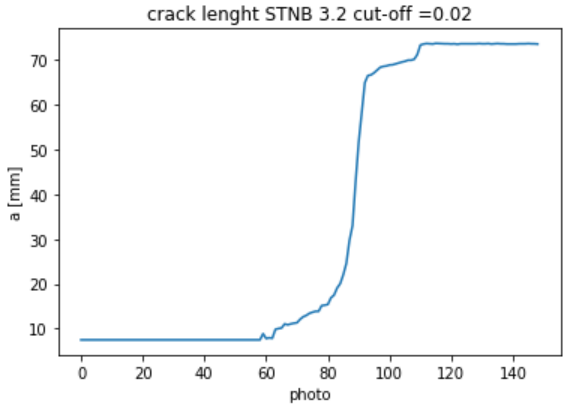

(b) crack length STNB-3, photo was taken every 500 cycles

Figure 5.5: Results fatigue tests STNB-3

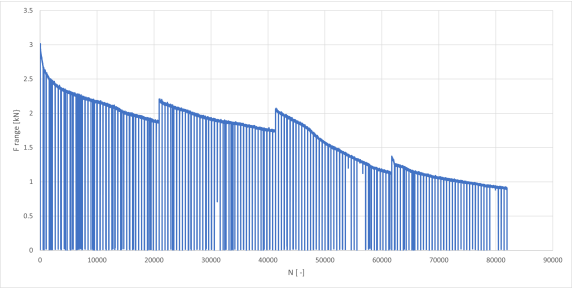

(a) TNB-4 incremental increasing displacement controlled, Force range vs cycles, R = 1

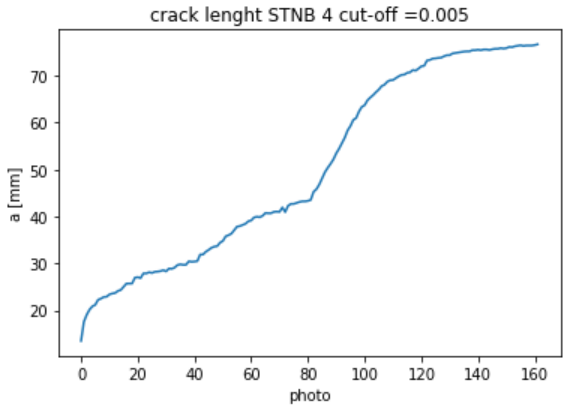

(b) crack length STNB-4, photo was taken every 500 cycles

Figure 5.6: Results fatigue tests STNB-4

linear correlation on the log-log plots for part of the data. Further investigation of these data shows that the linear correlation is in the parts before the unstable crack growth, which lies outside stage II crack where the Paris Law holds. When completely removing the data from the plots, two linear parts can be found. This data also shows agreement between the two tests. STNB 4 showed a much more stable crack growth during the testing. However, the resulting Paris curve has a large cluster of dots followed by a decreasing linear correlation. because of the decreasing correlation, no Paris law is given for this test. The difference between the first two tests and the last is really interesting.

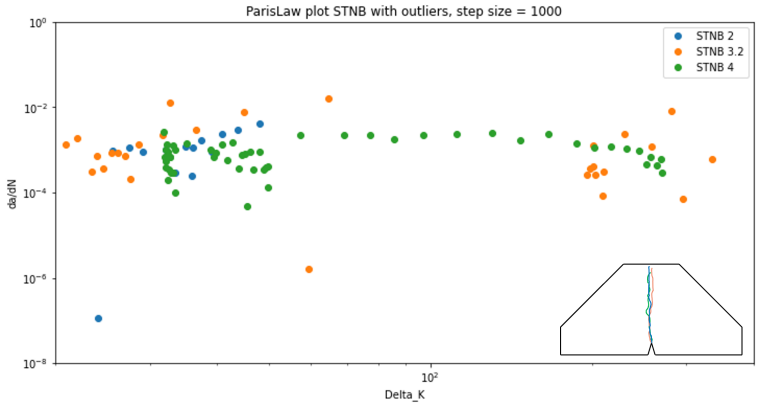

Figure 5.7: STNB Paris curves data

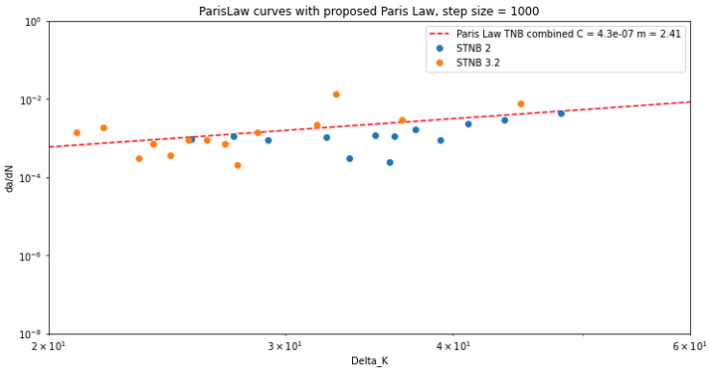

(a) STNB Paris law stage II data STNB 2 and 3

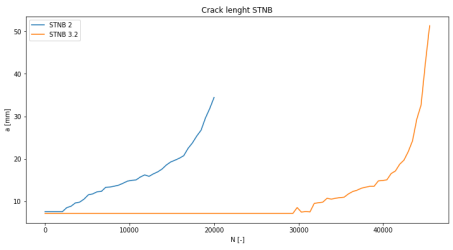

(b) Crack length stage II crack STNB 2 and 3

Figure 5.8: Paris law SRR using STNB

5.4. Microscope inspection of crack surface

To give an indication of the effect of fatigue failure on the material structure the crack surface where inspected using a small digital microscope. The crack surface of STNB 2,3 and 4 were compared with the crack surface of STNB 1 which failed under a ramping force. figure 5.9 shows the crack surfaces. three different surface parts can be indicated. clear reflecting SS, dark resin and yellow/brown hazy resin parts. The first two are failures between the SS and resin where the SS releases from the resin. it is assumed that the yellow/brown hazy parts are parts where the crack branches or has micro cracking around underlying SS. This leads to light deflecting in the resin resulting in a hazy look. Air voids along the crack path are hard to detect because they will show much in common with resin where the SS was released. From the pictures it is clear that the crack path is mostly between the SS and resin with some resin failure to link the parts.

Comparing the static crack surface with the fatigue crack surfaces it becomes apparent that the fatigue surface shows a lot more hazy parts than the static crack surface. For STNB 2 and 3 this is mostly in the start and middle. As expected when looking at the crack propagation. STNB 4 shows the dominant resin failure over all the parts. This seems to agree with the hypotheses that the fatigue cracking in SRR has the same process as with concrete where the fatigue loading results in micro-cracking around the SS followed by crack propagation with the linking of these micro-cracks.

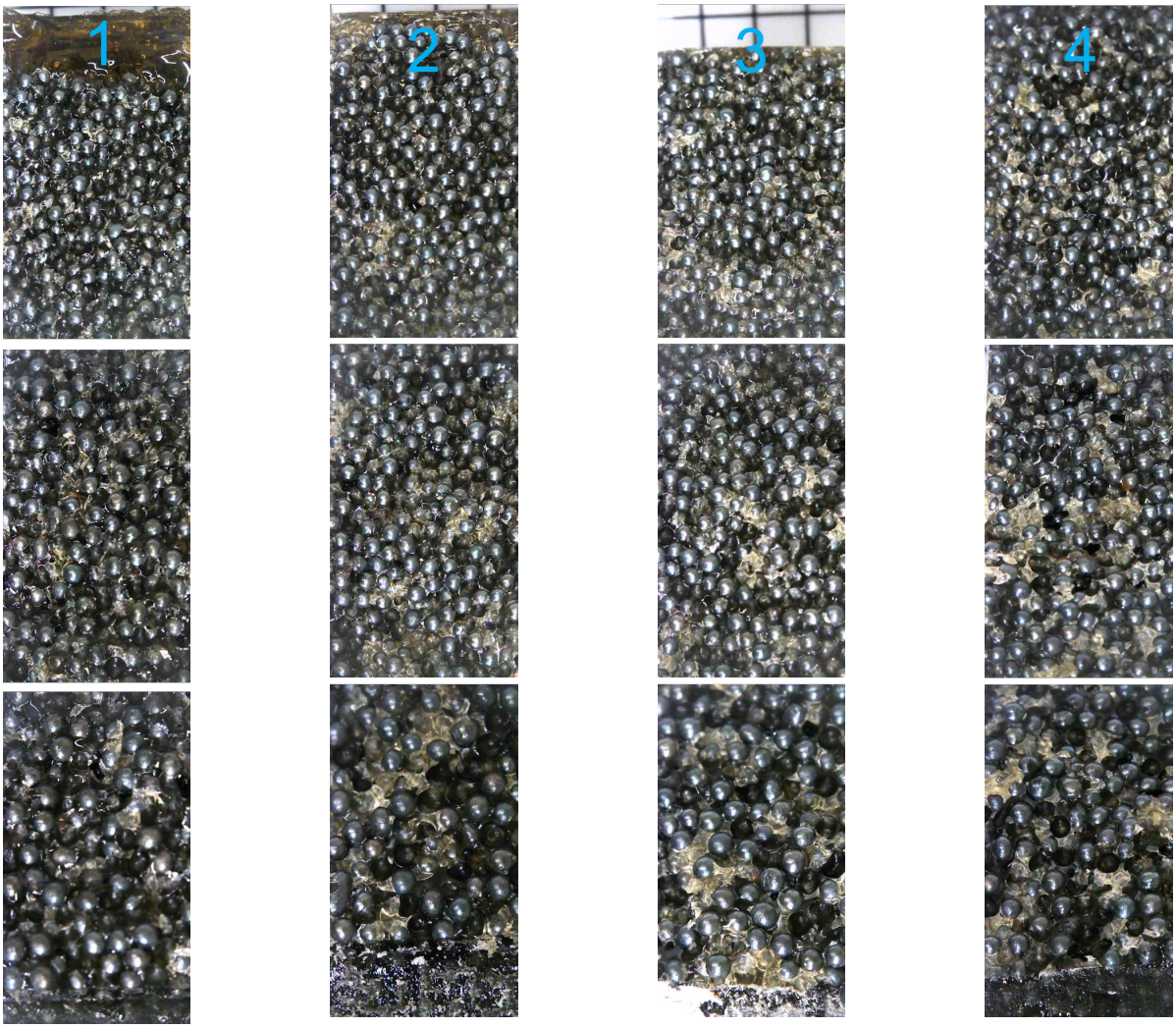

(a) STNB 1 static testing

(b) STNB 2 fatigue testing

(c) STNB 3 fatigue testing

(d) STNB 4 fatigue testing

Figure 5.9: Microscope pictures STNB, from top to bottom it shows: crack end, crack middle, crack start

5.5. Discussion and conclusions

Compared to the 2TCT tests the 3 point bending tests show a lot less deviation of the crack path. This could be caused by the increase in thickness or by the difference in form. The thicker specimen leads to less influence of possible voids on the crack path. The loading on the specimen forces the crack to end up close to the loading point. This reduces the chance of large deviation of the crack paths. The thinner SCB specimens did also show this behaviour. Next to this, the forces measured are a lot higher than in the 2TCT. The reason for this is clearly the difference in form as mentioned in the static analysis.

The sudden cracking does leave some concerns for the 3 point bending testing method. In an attempt to prevent this the sharper crack tip was added. The effect was phenomenal with stable crack propagation in all increments. The reason for this is not completely clear. Before the crack length was found it was assumed that the sudden increase in crack growth was caused by the energy build-up in the specimen which was released when the crack started. The blunt crack tip would cause the need for higher forces to start crack growth. Because the crack tip would be sharper after crack initiation the speed of crack propagation could be higher even with lower forces. Together with theoretical micro cracks in front of the crack tip. Which would be influenced further away the crack tip the blunter the crack tip would be. The blunt crack tip could have caused the sudden increase in the growth rate.

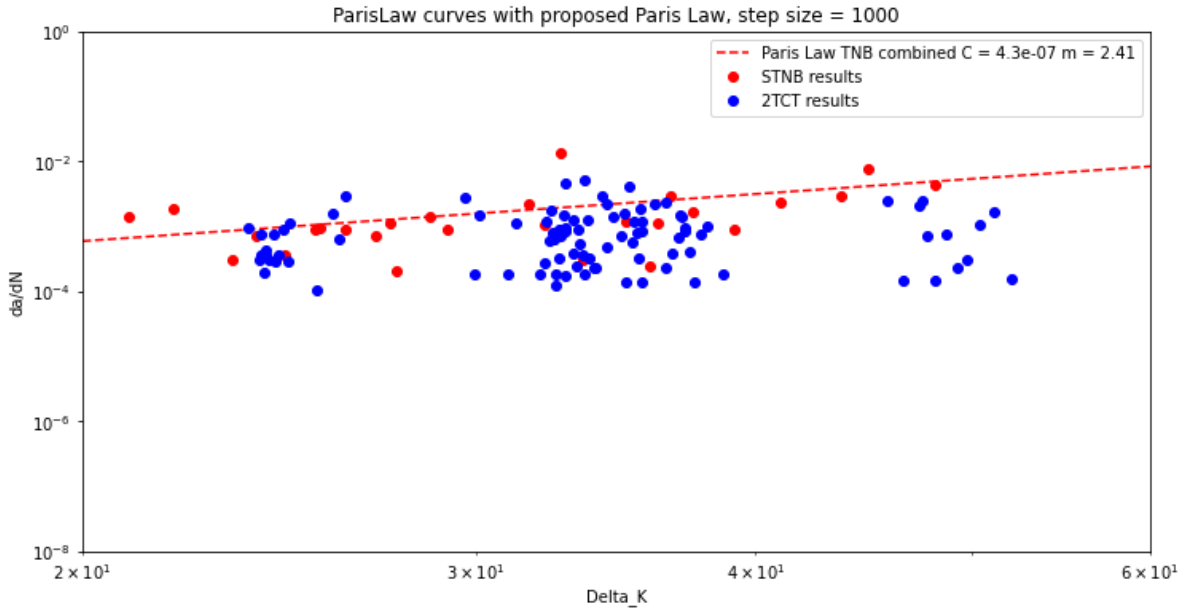

Figure 5.10: Proposed Paris law plotted on STNB and 2TCT experimental results in K range of 20 - 60

However, it is clear that the crack is already initiated before the unstable crack growth. Still, some of the mentioned effects could influence the sudden crack growth rate.

But, even with the unstable crack growth parts, the stable crack growth in the testing showed a linear relation where Paris Law parameters could be found. The STNB-2 and STNB-3 show the most consistent results. This would suggest C = 3.81e-10 and m = 4.18 or C = 1.76e-7 and m = 2.83. combining these two Paris plots to find one agreeable Paris law for the SRR with $R = 0$, $Hz = 1$ and $T = 25°$ results in C = 4.3e-7 and m = 2.41. figure 5.10 shows this Paris law shows compared to all the test results. The proposed Paris law seems to give, although a bit high, good results for K in the range 20 - 60. That the resulting Paris curve is on the high sight also makes it more conservative which is preferable with the high spread of the data.

The decreasing correlation of STNB 4 can be explained by the earlier mentioned theory on the lower amount of micro cracks further away from the crack tip. This would result in a higher stress intensity factor needed for crack growth. Combining this with the extrinsic mechanisms [38] found in SRR, meandering, crack deflection and wedging, as seen in the testing. This will lead to a rising R-curve where the crack growth rate decreases with an increasing crack length for certain crack lengths.

6

Numerical models

In this chapter numerical models will be used to validate the analytical formulas for the stress intensity factors (SIF) of the doubly tapered compact tension (2TCT) and short tapered notch beam (STNB) specimen. First a static model will be validated on the displacement in the 2TCT testing using digital image correlation (DIC) results . Then three xFEA model are made. The first one is on the 2TCT specimen to validate the xFEM by comparing the results with the standardised stress intensity factor and to research the mesh sensitivity of the stress intensity factor models. The other two models are used to validate analytic formulas for the stress intensity factors from literature presented in chapter 2.3. This is necessary because both of the forms have modifications from the original compact tensions (CT) and semi circular bending (SCB) shapes where the formulas are based on. These modification could influence the correctness of the analytical formulas. The J-intergral, VCCT and xFEM method all are valid to perform this check, yielding similar results [[4],[29]]. The xFEM method was preferred over the J-integral and VCCT because it had less re-meshing of the specimen for every crack length and the models could be largely reused if any fatigue xFEA was desired.

6.1. Description static model

For the static model a 3D solid extrusion is used. The dimensions are based on 2TCT specimen 15 with a thickness of 7.8mm, as shown in figure 6.1a. Linear elastic material properties are used based on table 3.2. For convenience of the data extraction the top and bottom support gaps are connected to a reference point in the centre of the gap by tie constrains coupling every degree of freedom to the reference point. The boundary conditions of the supports model the pin supports of the tests.To achieve this the bottom support only allows rotation around the $zaxis$ and the top support rotations around the $zaxis$ and translation in the $yaxis$. The boundary conditions are enacted on the reference points. The model is loaded with a concentrated force of $471Ninydirection$ based on the maximum force found during the 2TCT 15 test. Using partitions on the top face of the model the mesh is generated with nodes approximately $-18mminxdirection$ from the supports and 26 mm distance between the two. These nodes are used to validate the displacement in the specimens to the displacement in the specimen during the first loading of the test.

Young's modules [Mpa]	16200
Poison's ratio	0.13

Table 6.1: material parameters for static model

6.2. Results and comparison static model

From the model prescribed above the maximum displacement of the top supports found is 0.062 mm. From the DIC a displacement of the top support of 0.111 mm was found while the testing machine reported a displacement of 0.20 mm. To find an accurate comparison between the model and the test the DIC figures are used. The displacement in y during the first loading of two points 18 mm from the

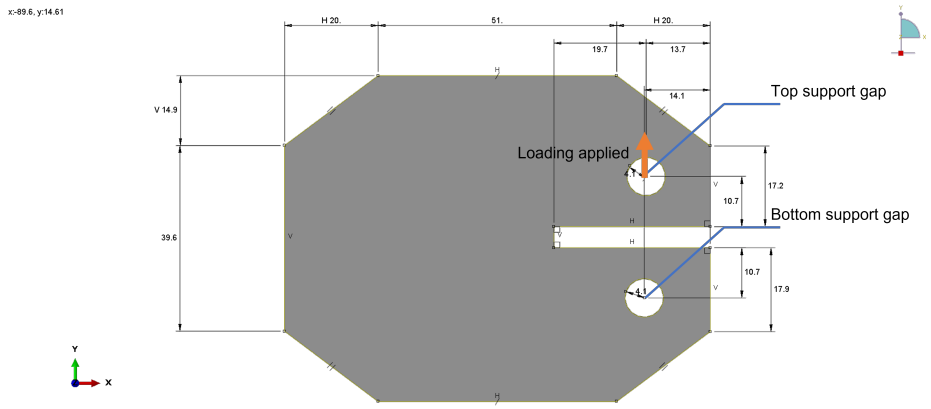

(a) Dimensions in mm thickness = 7.8mm

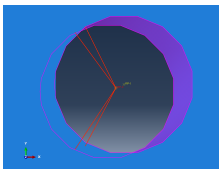

(b) Tie constraint used in pin supported models

Figure 6.1: Abaqus model 2TCT

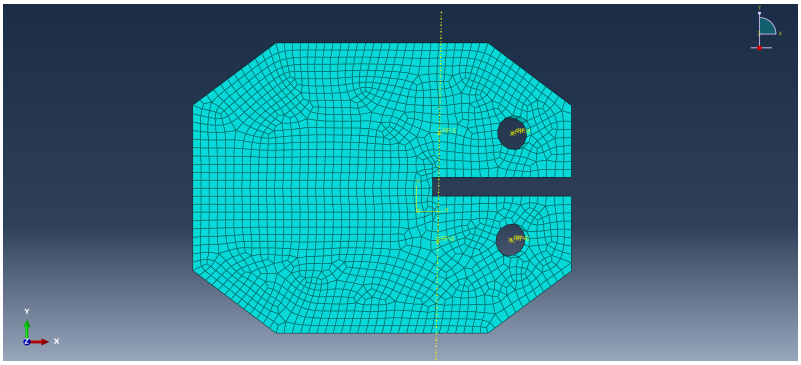

Figure 6.2: partitioned mesh static model 2TCT

Average mesh size	2x2x2 mm
Number of elements	1700
Number of nodes	3602
Geometric Order	Linear
Element geometry	Hexahedral
Element type	8-node linear brick, reduced integration, hourglass control (C3D8R)

Table 6.2: mesh properties static model

supports and 26mm between each other is measured. To validate the stiffness of the model the difference between the displacement in y of the two points is compared with the difference in displacement in y of the same points in the Abaqus model. The DIC results in 0.03 mm difference in displacement, the Abaqus model 0.016mm. Reducing the mesh size does lead to a small increase in displacement difference with 1 mm mesh size resulting in 0.018 and 0.5 mm mesh size in 0.019. Changing the model to a displacement loaded model has no effect on the found displacement.

6.3. Conclusion static model

The discrepancy found between the testing machine reported displacement and the DIC displacement probably has to do with the inaccuracy in the machine due the secondary effects influencing the displacement measuring. The model leads to about 1.5-2 times stiffer results than the DIC does for both the support displacement and the resulting points. This could be caused by a couple of factors. Firstly, it could be that the stiffness achieved in the specimens is indeed 1.5-2 times lower than the stiffness found in the research by A. Christoforidou et at. A couple of steps differ between the production in the mentioned research and in this research: the change of Lupranate used in the production of the SRR

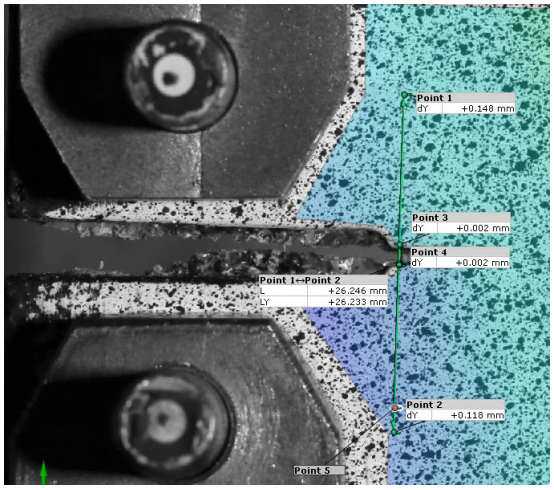

Figure 6.3: DIC values for stiffness validation

could have this effect on the stiffness, the thicker specimens or the vibration of the specimens could have reduce the influence of any voids on the stiffness and lastly the post-curing of the specimen could lead to the higher stiffness measured by A. Christoforidou et at. [11]. Other reason for this discrepancy between the two results could be in the testing. The fork used to load the specimen was free to move in y direction but the large arm also permitted some movement in x direction. The result of the movement in x direction is a misalignment in the loading points resulting in an angled specimen in the reference stage. When the specimens was loaded this misalignment was removed, but it did result in large extra displacement measured due to the angle that the specimen moved in. However, this rotation is only $0.0015°$ and the distance was taken between points close by the supports so the effect of this rotation on the y displacement is negligible.

6.4. Description SIF xFEM model

The models used for the SIF uses the same material properties and element types as the static model [6.1, 6.2]. The 2TCT and CT model do use the same tie constraints and boundary conditions around the supports. The STNB specimen in loaded and supported over 1mm width to prevent singularities at the supports and loading points, the left support is pinned and the right side is a roller. The CT and 2TCT are loaded under 2500 N in y direction. The STNB -2500 N in y direction. The dimensions use for the 2TCT and STNB are that of the ideal specimens, the CT specimen dimensions are taken from research [42]. The main difference are in the inclusion of a stationary crack and modification on the meshing. To find the SIF using a xfem model in Abaqus xFEM crack needs to be assigned. This crack is made by including a 3D shell extrusion part in the model. The crack part is put at the crack location in the assembly of the model. multiple authors [[4],[25]] indicate the importance that the the edges extend, see figure **??** for a close up. To find the contour integrals around the crack tip the crack in not allowed to grow. The SIF is found in the last increment of the the model in 5 contours using the maximum energy release rate as crack initiation criterion. Previous research shows that the first contour has a high variation on in the SIF and should be disregarded [19]. Because of the 5 contours it is important that at least 5 fine size mesh elements surround the crack tip. To accommodate the need for 5 fine mesh sized elements the mesh is refined around the crack path. This is done in such a way that the elements line up with the end of the crack tip. The mesh of the around the crack is 0.5 mm further away it is 2 mm in case of the 2TCT and CT and 5 mm for the STNB. Due to computational limitations only 1 element through thickness could be used for the 2TCT and CT models. The STNB uses 3 elements through thickness. 4 Different crack lengths varying between the specimens where used to compare the SIF from Abaqus with the analytical formulas, see table 6.4.

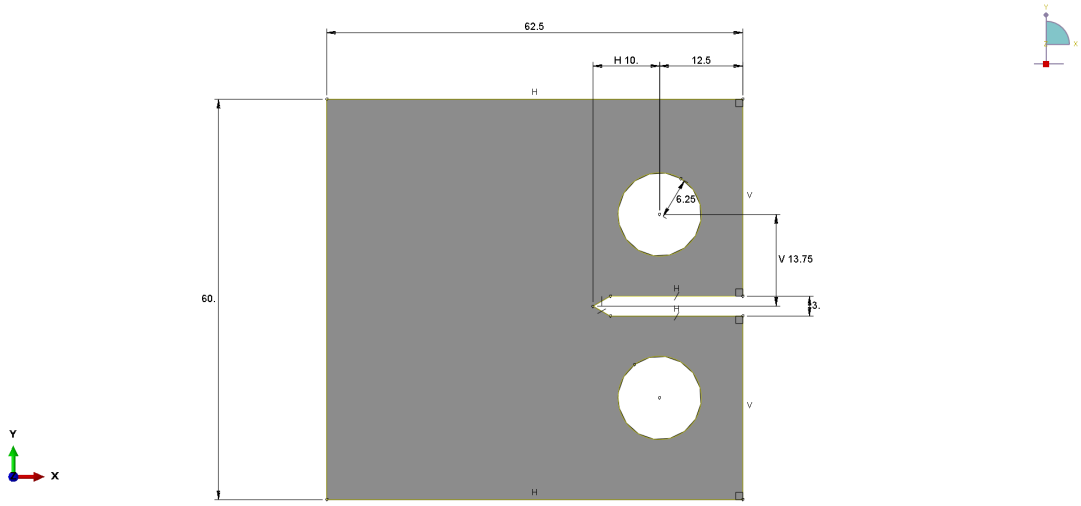

(a) CT dimensions in mm thickness = 4mm

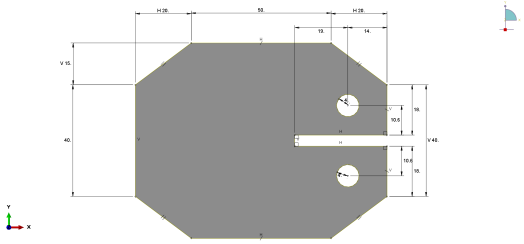

(b) 2TCT dimensions in mm thickness = 7.5mm

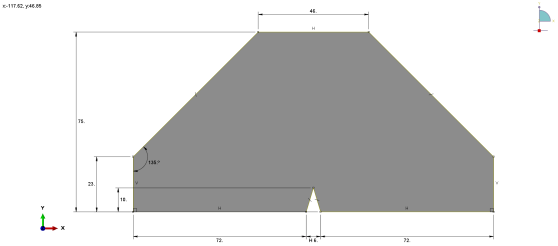

(c) STNB dimensions in mm thickness = 20mm

Figure 6.4: Dimensions of SIF models

	2TCT	CT	STNB
number of elements	6946	3893	24177
number of nodes	14114	7994	32556

Table 6.3: Mesh SIF models

6.5. Comparison between CT SIF model and analytical formula

To compare the model SIF to the analytical formula the average between contour 2 to 5 was taken and plotted. See figure 6.7 for the found results. From this it is clear that the Abaqus model slightly overestimates the SIF. With a growing difference when the SIF increases. This is in agreement with various research. In research done by S. Courtin et at. the SIF found using various 3D FEM was higher than found with empirical expressions [13]. Research done by J.W.Hu using the J-integral method showed good agreement between the 2D model and the ASTM formula. The 3D model showed higher deviation between the contour integrals and a total higher SIF than the 2D model. Varying from about 8% to 11% depending on the load displacement applied [19].

Furthermore, when exploring the mesh sensitivity of the model, decreasing the mesh size leads to a lowering of the SIF, see figure 6.8. With a decrease of 3.13% between the maximum SIF's. The large mesh sizes not only lead to higher averages but also a high deviation between the contours, further

	crack length 1 [mm]	crack length 2 [mm]	crack length 3 [mm]	crack length 4 [mm]
CT	15	25	30	35
2TCT	25	35	55	65
STNB	15	25	45	60

Table 6.4: Crack lengths used to find SIF

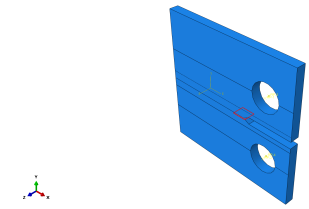

(a) Overview extended crack part

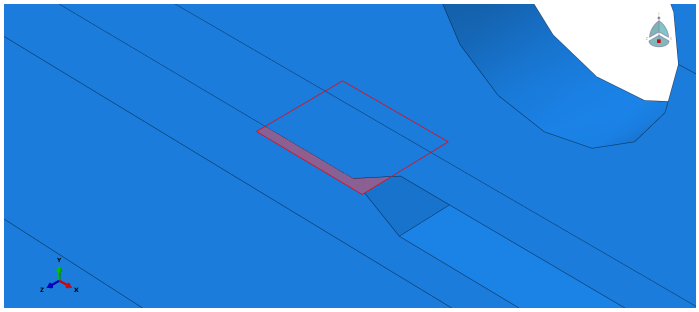

(b) close up extended crack part

Figure 6.5: extended crack part

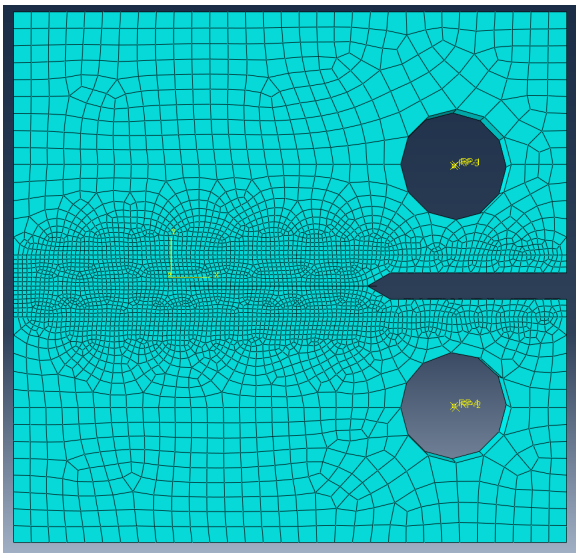

(a) CT mesh

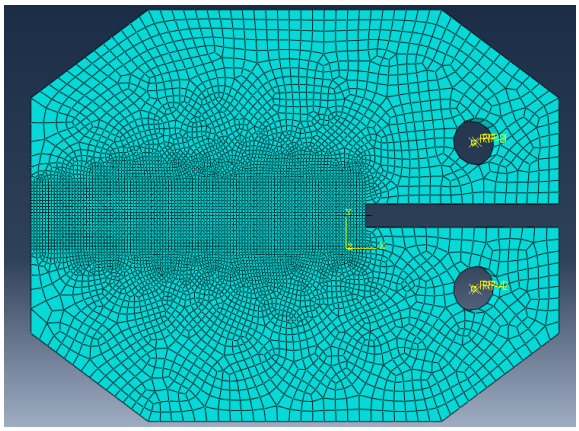

(b) 2TCT mesh

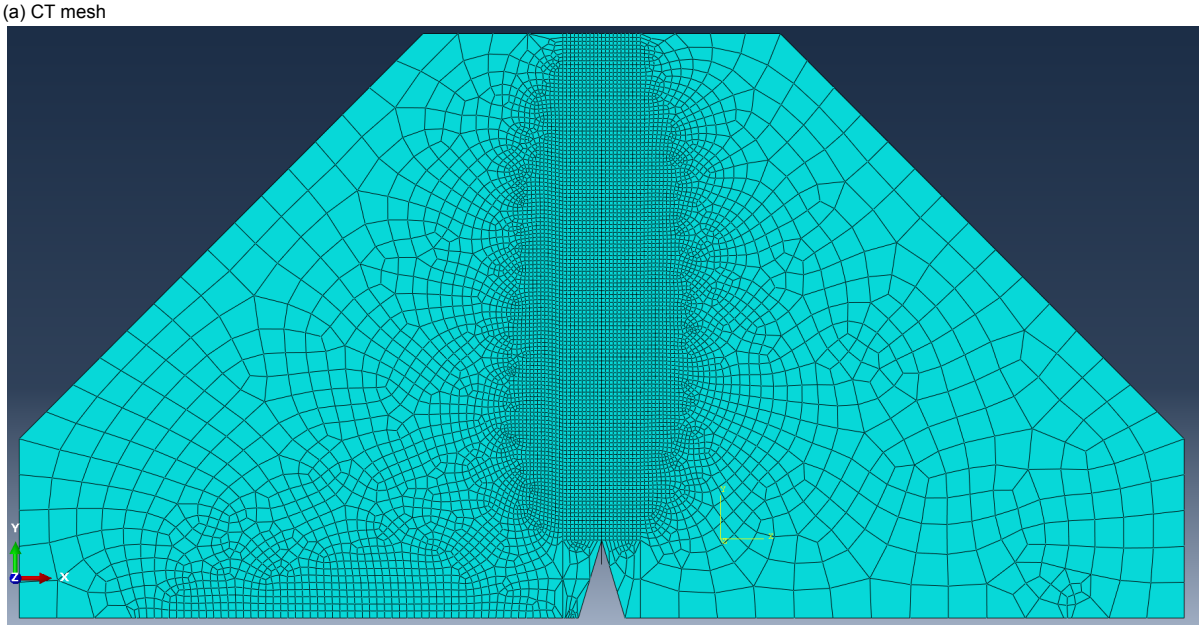

(c) STNB mesh

Figure 6.6: Mesh for xFEM SIF analysis 0.5mm around crack region

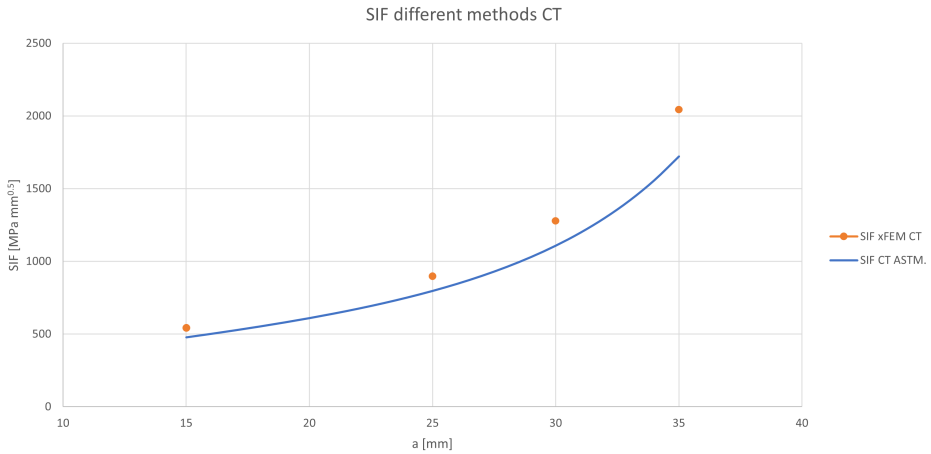

Figure 6.7: SIF vs a [mm] of xFEM and ASTM standard

indicating the importance of the 5 fine sized element around the crack tip. The research done by J.W. Hu used multiple elements through thickness [19]. This will drastically decreases the mesh size and further reduce the SIF found to be more in agreement with the ASTM.

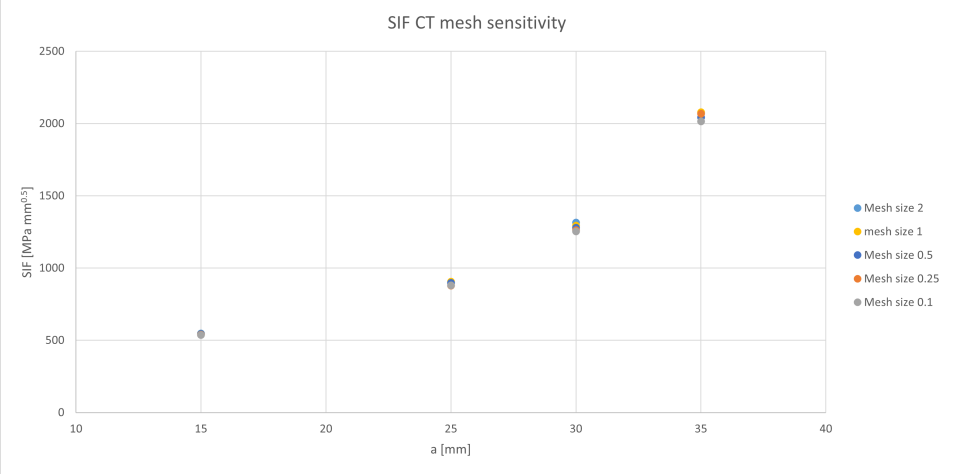

Figure 6.8: SIF vs a [mm] of different mesh sizes

The SIF had a 1.4% difference between 0.5 mm mesh and 0.1 mm. But, with a 20x longer computation time the decision was made to use 0.5 mm mesh for the 2TCT and STNB models. Even though the results where higher than the ASTM formula the model is assumed to work correctly because the difference is relatively small and was also found in various other research when working with 3D models.

6.6. Comparison between 2TCT, STNB SIF models and analytical formulas

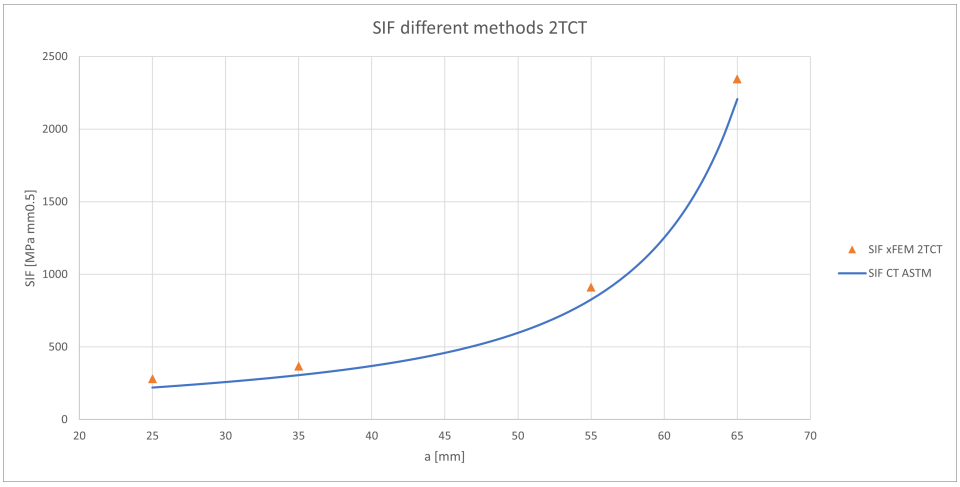

Figure 6.9: SIF vs a [mm] of xFEM and CT ASTM standard

The 2TCT model again shows the overestimation as found in the CT model. The main difference is that the fraction the ASTM is overestimated it is decreasing in the 2TCT specimen, while in the CT specimen it increased. from 26.8% to 6.3% for 2TCT and from 13.5% to 18.7% for CT. If the correct formula to find the SIF would be the same for the CT and the 2TCT specimens it would be expected that the same pattern in the overestimation would be found. This not being the case in this specimen configuration could indicated that even though the analytical formula gives good results a better formula could be found for the 2TCT specimen. However, the difference could also stem from the difference in W/B in the specimens.

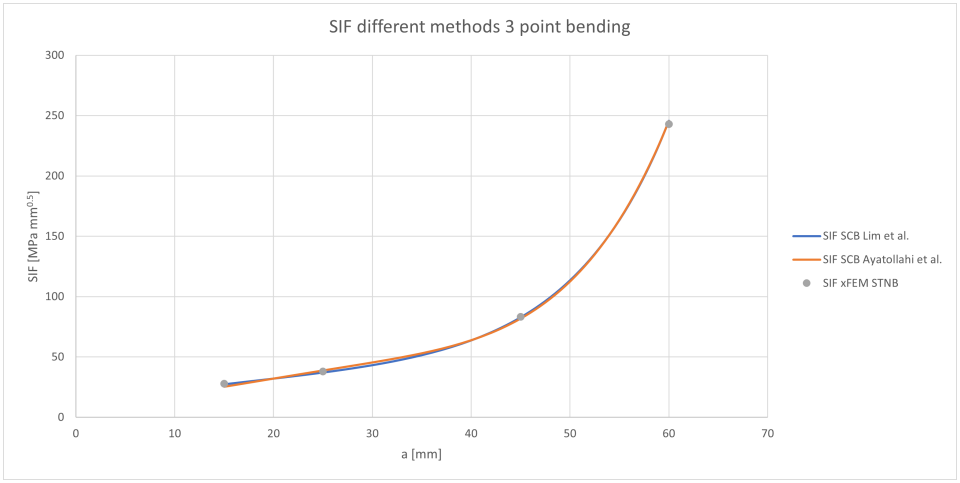

Figure 6.10: SIF vs a [mm] of xFEM and formula for SCB from literature [[26],[6]]

The STNB was compared with the analytical formula introduced in equation 2.10 and as extra check to equation 6.1. Which gives the SIF for any SCB specimen configuration [6].

$$K = ((P_{max} * \sqrt{\pi * a})/2RB) * (0.1422 + 5.06355(S/R)) + (-16.65 + 3.319(S/R))\alpha + (52.939 + 76.910(S/R))\alpha^2 + (-67.027 - 257.726(S/R))\alpha^3 + (29.247 + 252.8(S/R))\alpha^4 \quad (6.1)$$

- where α is the ratio of the crack length on the radius

The STNB model shows commensurate results to the analytical formulas. The cause of this could be twofold. Firstly this model used more element through thickness which was not possible in the 2TCT and CT specimen. Secondly the method that the analytical formulas are derived from is comparable to the numerical method used. The ASTM standard uses a formula obtained by boundary collocation analysis [[30], [46]] were for both SCB formulas FEA data is used to fit the analytical formula [[26], [6]].

6.7. Conclusion on the SIF results

The xFEM model on the CT gives similar results for the SIF compared to the ASTM standard as multiple other research's using 3D J-integral have shown [[19], [13]]. The 3D are known to lead to an slight overestimation of the SIF. So, the modeling method is expected to give good results when applied to compare the modified specimens forms to the suggest analytical formulas. The results show excellent agreement between the SCB formulas and the STNB model. With exception of the crack length of 15mm for equation 6.1, both formulas have results within 2% of the model. At the small crack length equation 6.1 shows higher variation, thus using equation 2.10 for this specific specimen configuration leads to the best results. In the 2TCT model the overestimation was again found. The difference in pattern suggests that the a slight alteration too the formula could lead to better results. However, the results where still rather similar to the ones found using equation 2.6, which seems adequate to predict the SIF for 2TCT specimens.

7

Conclusion

In this thesis experimental testing on both the compact tensions specimens and the 3 point bending specimens, numerical research on the stress intensity factor using Abaqus and the production of the complicated forms it performed. The following conclusions can be drawn based on the performed work:

- For the production of complicated forms in SRR, the best results are achieved by closed mould injection casting and ring mould injection casting. With an average difference between intended dimensions and specimen dimensions of 0.22 mm for CMIC and 3.13 mm for RMIC and an average standard deviation between the specimens of 0.40 mm and 0.87 mm the production methods are precise. Together with only 1 in 10 specimens showing any surface imperfection. The casting methods result in accurate and consistent specimens.
- The 3 point bending test setup using the short tapered notched beam specimen shows better results for the study of fatigue crack propagation of SRR compared to compact tensions test setup using doubly tapered notched beam specimens. Less scatter in the resulting crack growth plots is found. furthermore the crack path deviates only 4.27 % of the width of the specimen, compared to 38.86 % in the case of compact tensions specimens.
- The incremental displacement loading results in a more stable crack growth than the load displacement controlled load type. Incremental displacement loading resulted in stable crack growth during at least 20000 loading cycles. The force controlled loading resulted in a maximum of 8000 cycles of stable crack growth.
- The analytical formula for the stress intensity factor for SCB specimens with span over diameter ratio of 0.8 proposed by Lim et al. [26] gives accurate results for the short tapered notch beam specimens with span over height ratio of 0.8, with a difference of 1.15% at crack length 15mm and 1.10% difference at crack length of 60mm.
- A linear correlation was found in the crack growth rate plots constructed from the short tapered notch beam tests, for K ranging from 20 till 60. From this linear correlation the fitting of the Paris Law resulted in $C = 4.3e - 7$ and $m = 2.41$ with a $R^2 = 0.44$. These results were obtained with steel reinforced resin using unsaturated polyester combined with polyurethanes mixed with 1mm steel shot to a weight percentage of 80% SS to resin.

.

8

Recommendations and discussion

For further research on the crack propagation of SRR it can be advised to work with silicon moulds. The flexibility and chemical resistance when working with these moulds is really beneficial for the casting experience. Also, the use of steel ring moulds is worth considering, in order to achieve sharper notches without the need of the paper induced notch. However, a method must be found on how to completely close the mould using glass plates. The use of professionally made moulds is something worth considering when the tests sample size is increased or when working with vacuumed specimens. It can also be advised to forego the desire to replicate in use SRR. Instead, try to achieve the least amount of imperfections as possible by including shaking or pressurizing the specimens. The imperfections and expected voids resulted in high scattering of the data, which made processing difficult. The consistency can probably be increased by first trying to find results with perfect conditions. Factors can always be applied to make it presentable in design codes. When working with materials where the crack propagation is unknown, the use of incremental increasing displacement controlled tests can greatly speed up the testing setup. Working around the cut off limits and crack initiation can have this effect as well. The SRR did show a problem where the stiffness loss of the material in displacement controlled testing resulted in R of exactly 0. Leave every cycle resulting in a moment of impact when the load was started again. To prevent this a solution could be to combine loading and displacement controlled testing. In such a test, the maximum load can be governed by displacement control and the minimum by force control. Research on the feasibility and the apply method would be needed for this.

The use of loading combined with displacement controlled testing is one of the things further research could be done for to increase the usability of crack propagation testing in SRR. Other topics that can be researched are:

- The effect of the steel shot on the curing of the resin to indicate any possible effect of an interfacial transition zone. This will lead to a more in depth understanding on the failure in the microstructure of the SRR
- More detailed investigation of the crack surfaces of fatigue failed specimens using microscopic research could give more insight on the effect of stable fatigue failure vs unstable fatigue failure, as well as the cracking around steel shot, the possible interfacial transition zone and cracking around voids.
- The void content of specimens produces is another topic of interest. This could be investigated in the tested specimens to link the crack propagation to the void content and the surface imperfections to the void content. One method for this could be using computed tomography.
- Lately providing an improved analytical formula for the modified CT specimen 2TCT could provide an interesting study when extensive use of this modified form is made. Predict the SIF more accurate could reduce the stress intensity factor found in the testing.

Bibliography

[1] July 2014. URL: https://www.compresdev.co.uk/CRD%5C%20The%5C%20Use%5C%20and%5C%20Application%5C%20of%5C%20Epoxy%5C%20Resin%5C%20vs%5C%20Vinylester%5C%20vs%5C%20Polyester.pdf.

[2] .

[3] .

[4] Laura Aboltina. Feb. 2022. URL: http://resolver.tudelft.nl/uuid:0b572817-73bc-44b7-8219-0dc774d79018.

[5] K Amelink. *Betrouwbare Bruggen voor een Bereikbaar Nederland*. June 2015. URL: https://puc.overheid.nl/rijkswaterstaat/doc/PUC_167708_31/.

[6] M. R. Ayatollahi et al. "Stress intensity factors of semi-circular bend specimens with straight-through and Chevron notches". In: *Rock Mechanics and Rock Engineering* 49.4 (2015), pp. 1161–1172. DOI: 10.1007/s00603-015-0830-y.

[7] Lawrence Colin Bank. *Composites for construction: Structural design with FRP Materials*. John Wiley and Sons, 2006.

[8] BASF.

[9] Hamid Behbahani and Reza Salehfard. "A review of studies on asphalt fine aggregate matrix". In: *Arabian Journal for Science and Engineering* 46.11 (2021), pp. 10289–10312. DOI: 10.1007/s13369-021-05479-w.

[10] N. Blanco et al. "Intralaminar fracture toughness characterisation of woven composite laminates. part I: Design and analysis of a compact tension (CT) specimen". In: *Engineering Fracture Mechanics* 131 (2014), pp. 349–360. DOI: 10.1016/j.engfracmech.2014.08.012.

[11] Angeliki Christoforidou, Ron Verleg, and Marko Pavlovic. "Durability of reinforced resins based on static, fatigue, and water absorption tests". In: ().

[12] Héctor Cifuentes et al. "Modified disk-shaped compact tension test for measuring concrete fracture properties". In: *International Journal of Concrete Structures and Materials* 11.2 (2017), pp. 215–228. DOI: 10.1007/s40069-017-0189-4.

[13] S. Courtin et al. "Advantages of the J-integral approach for calculating stress intensity factors when using the commercial finite Element Software abaqus". In: *Engineering Fracture Mechanics* 72.14 (2005), pp. 2174–2185. DOI: 10.1016/j.engfracmech.2005.02.003.

[14] F. Csillag. 2018.

[15] *Elastosil Vario 40 + cat. Vario N / Siliconen additie transparant 40*. URL: https://www.siliconesandmore.com/nl/wacker-elastosil-vario-40-catalyst-vario-normaal.html.

[16] *Fatigue crack growth and life prediction*. URL: https://engineeringlibrary.org/reference/fatigue-crack-growth.

[17] *Fatigue crack growth rate graph*. Nov. 2017. URL: https://kb.appinc.co/knowledge-base/under-pressure-material-failure-due-to-fatigue/fatigue-crack-growth-rate-graph-jpgt1511197644305width640namefatigue-crack-growth-rate-graph/.

[18] Ameer A. Hilal. "Microstructure of concrete". In: *High Performance Concrete Technology and Applications* (2016). DOI: 10.5772/64574.

[19] Jong Wan Hu. "J-integral evaluation for calculating structural intensity and stress intensity factor using commercial finite element (fe) solutions". In: *Advanced Materials Research* 650 (2013), pp. 379–384. DOI: 10.4028/www.scientific.net/amr.650.379.

[20] Victor Igwemezie, Ali Mehmanparast, and Feargal Brennan. “The influence of microstructure on the fatigue crack growth rate in marine steels in the paris region”. In: *Fatigue and Fracture of Engineering Materials and Structures* 43.10 (2020), pp. 2416–2440. DOI: 10.1111/ffe.13312.

[21] Kamil E Kaloush. “A notched disk crack propagation test for Asphalt Concrete”. In: *MOJ Civil Engineering* 3.5 (May 2017). DOI: 10.15406/mojce.2017.03.00084.

[22] J. Karger-Kocsis and K. Friedrich. “Microstructure-related fracture toughness and fatigue crack growth behaviour in toughened, anhydride-cured epoxy resins”. In: *Composites Science and Technology* 48.1-4 (Jan. 1993), pp. 263–272. DOI: 10.1016/0266-3538(93)90143-5.

[23] Subramaniam V. Kolluru et al. “Crack propagation in flexural fatigue of concrete”. In: *Journal of Engineering Mechanics* 126.9 (2000), pp. 891–898. DOI: 10.1061/(asce)0733-9399(2000)126:9(891).

[24] Sharvan Kumar and William A. Curtin. “Crack interaction with microstructure”. In: *Materials Today* 10.9 (2007), pp. 34–44. DOI: 10.1016/s1369-7021(07)70207-9.

[25] Michael Levén and Daniel Rickert. 2012. URL: https://publications.lib.chalmers.se/records/fulltext/164269.pdf.

[26] I.L. Lim, I.W. Johnston, and S.K. Choi. “Stress intensity factors for semi-circular specimens under three-point bending”. In: *Engineering Fracture Mechanics* 44.3 (1993), pp. 363–382. DOI: 10.1016/0013-7944(93)90030-v.

[27] Luis Lorenzo and H. Thomas Hahn. “Effect of ductility on the fatigue behavior of epoxy resins”. In: *Polymer Engineering and Science* 26.4 (1986), pp. 274–284. DOI: 10.1002/pen.760260403.

[28] Nick McCormick and Jerry Lord. “Digital Image Correlation”. In: *Materials Today* 13.12 (2010), pp. 52–54. DOI: 10.1016/s1369-7021(10)70235-2.

[29] Toshio Nagashima, Youhei Omoto, and Shuichi Tani. “Stress intensity factor analysis of interface cracks using X-FEM”. In: *International Journal for Numerical Methods in Engineering* 56.8 (Apr. 2002), pp. 1151–1173. DOI: 10.1002/nme.604.

[30] JC Newman. “Stress analysis of the compact specimen including the effects of pin loading”. In: *National Symposium on Fracture Mechanics* (1974). DOI: 10.1520/stp33136s.

[31] T. Niendorf et al. “On the fatigue crack growth–microstructure relationship in ultrafine-grained interstitial-free steel”. In: *Journal of Materials Science* 45.17 (2010), pp. 4813–4821. DOI: 10.1007/s10853-010-4511-7.

[32] M.P. Nijgh. *A multi-scale approach towards reusable steel-concrete composite floor systems*. 2021. URL: https://doi.org/10.4233/uuid:983b06e7-c30b-465c-a032-2439a7e9863f.

[33] Gerhard Olivier et al. “Feasibility of bolted connectors in hybrid FRP-steel structures”. In: *Lecture Notes in Civil Engineering* (2021), pp. 1055–1064. DOI: 10.1007/978-3-030-88166-5_92.

[34] M J Owen and R G Rose. “The fracture toughness and crack propagation properties of polyester resin casts and laminates”. In: *Journal of Physics D: Applied Physics* 6.1 (Jan. 1973), pp. 42–53. DOI: 10.1088/0022-3727/6/1/309.

[35] DR Petersen et al. “Development of a single-edge notched beam test for asphalt concrete mixtures”. In: *Journal of Testing and Evaluation* 33.6 (Nov. 2005), p. 12579. DOI: 10.1520/jte12579.

[36] Aravind Ramkumar. Aug. 2021. URL: https://repository.tudelft.nl/islandora/object/uuid:df4c2ad5-2838-409b-aa7c-b63dae5737a8?collection=education.

[37] Hans W. Reinhardt, Hans A. Cornelissen, and Dirk A. Hordijk. “Tensile tests and failure analysis of concrete”. In: *Journal of Structural Engineering* 112.11 (1986), pp. 2462–2477. DOI: 10.1061/(asce)0733-9445(1986)112:11(2462).

[38] R.O. Ritchie. “Mechanisms of fatigue crack propagation in metals, ceramics and composites: Role of crack tip shielding”. In: *Materials Science and Engineering: A* 103.1 (1988), pp. 15–28. DOI: 10.1016/0025-5416(88)90547-2.

[39] R.O. Ritchie. “Mechanisms of fatigue-crack propagation in ductile and brittle solids”. In: *International Journal of Fracture* 100 (1999), pp. 55–83.

[40] P. Romero and E. Masad. “Relationship between the representative volume element and mechanical properties of asphalt concrete”. In: *Journal of Materials in Civil Engineering* 13.1 (2001), pp. 77–84. DOI: 10.1061/(asce)0899-1561(2001)13:1(77).

[41] Elio E Saenz et al. “Fatigue crack propagation in polyvinylchloride and polyethersulfone polymer foams”. In: *Journal of Sandwich Structures and Materials* 16.1 (2013), pp. 42–65. DOI: 10.1177/1099636213505304.

[42] Ravi Shankar Gupta. July 2019. URL: http://resolver.tudelft.nl/uuid:ef98f2f7-aa79-4bd1-b444-be8c2915eafe.

[43] *SIMULIA User Assistance 2021*. URL: https://help.3ds.com/2021/English/DSSIMULIA_Established/SIMULIA_Established_FrontmatterMap/sim-t-SIMULIA_EstablishedDocSearchOnli htm?contextscope=all&id=b0d455eac2894a22afb699b26f2c21d9.

[44] M.A. Sokolov. 2017.

[45] AOC trusted Solutions.

[46] John E. Srawley. “Wide range stress intensity factor expressions for ASTM E 399 standard fracture toughness specimens”. In: *International Journal of Fracture* 12.3 (1976), pp. 475–476. DOI: 10.1007/bf00032844.

[47] “Standard Test Method for Mearurement of Fatigue Crack Growth Rate”. In: *ASTM Compas* (May 2015). DOI: 10.1520/e0647-15e01. URL: http://astm.com/.

[48] Stephen A. Sutton. “Fatigue crack propagation in an epoxy polymer”. In: *Engineering Fracture Mechanics* 6.3 (1974), pp. 587–595. DOI: 10.1016/0013-7944(74)90015-0.

[49] K Tanaka. “Mechanics and Micromechanics of Fatigue Crack propagation”. In: *Fracture Mechanics: Perspectives and Directions (Twentieth Symposium)* (1989). DOI: 10.1520/stp18824s.

[50] *The Glass Transition*. 2003. URL: https://web.archive.org/web/20190115195943/http://pslc.ws/macrog/tg.htm.

[51] Levent Tutluoglu and Cigdem Keles. “Mode I fracture toughness determination with straight notched disk bending method”. In: *International Journal of Rock Mechanics and Mining Sciences* 48.8 (2011), pp. 1248–1261. DOI: 10.1016/j.ijrmms.2011.09.019.

[52] M. P. Wagnoner, W. G. Buttlar, and G. H. Paulino. “Disk-shaped compact tension test for asphalt concrete fracture”. In: *Experimental Mechanics* 45.3 (2005), pp. 270–277. DOI: 10.1007/bf02427951.

[53] Jian Wang. 2015.

[54] Xun Xi et al. “Modelling the crack initiation and propagation of notched rock beam under the three-point bending load”. In: *Advances in Civil Engineering* 2020 (2020), pp. 1–11. DOI: 10.1155/2020/8810023.

[55] Haohui Xin, Martin Nijgh, and Milan Veljkovic. “Computational homogenization simulation on steel reinforced resin used in the injected bolted connections”. In: *Composite Structures* 210 (2019), pp. 942–957. DOI: 10.1016/j.compstruct.2018.11.069.

[56] Xingyi Zhu et al. “Identification of interfacial transition zone in asphalt concrete based on nanoscale metrology techniques”. In: *Materials and Design* 129 (2017), pp. 91–102. DOI: 10.1016/j.matdes.2017.05.015.

A

Dimensions specimens

Specimen number	w [mm]	a0	t1	t2	a*	D	h1	h2	b1	b2	l1	l2	ov1	ov2	oh1	oh2	G [gr]	avg
2	75.35	20.55	7.7	7.7	34	8.1	40	69.6	49.8	88.8	18.3	18.2	6.2	6.2	9.3	9.5	182.7	
5	76.575	20.975	7.4	6.9	34.4	8.6	40	69.4	51.6	90	17.2	17.8	6.3	6.1	9	9.25	168.6	
6	74.75	20.45	7.6	7.3	34.1	8.2	40.5	69.7	50.6	88.4	18.2	17.9	6.4	6.7	9.8	9.3	192.4	
7	76.1	20.2	7.45	7.6	34.1	8.1	39.2	69.7	49.4	90	18	18	6.4	6.3	9.8	9.9	196.7	
8	75.4	20.7	7	6.9	34.3	8.3	41	70.5	49.5	89	18.1	18.2	6.9	6.5	9.3	9.6	184.1	
9	75.5	21.2	7.2	7.2	34.9	8.1	41	69.6	51.3	89.2	18.1	17.5	6.9	6.6	9.5	9.8	185.7	
10	74.875	20.275	7.1	7.1	34.3	8.35	40	70	49.8	88.9	18.4	18.3	6.9	6.6	10	9.7	178.9	
11	75.75	20.75	7.4	8.1	34.4	8.3	41.5	69.85	51	89.4	17.5	18.5	6.5	6.5	9.5	9.5	190.6	
12	75.725	20.325	7	7	34	8.35	41.4	69.9	50	89.4	18.1	18.8	6.75	6.5	9.3	9.7	177	
13	75.85	19.55	7.2	7.5	33.3	8.1	40	69.4	51.8	89.6	17.7	17.2	6.6	6.6	9.5	9.9	181.1	
14	76.15	20.25	8.1	8	34	8.3	39.5	69	52	89.9	18.5	17.9	6.8	6.6	9.6	9.6	212.1	
15	76.1	19.7	8	7.6	33.6	8.2	39.6	69.4	51	90	17.2	17.9	6.6	6.6	9.6	10	202.3	
avg	75.68	20.41	7.43	7.41	34.12	8.25	40.31	69.67	50.65	89.38	17.94	18.02	6.60	6.48	9.52	9.65	187.68	
STD	0.51	0.46	0.35	0.39	0.39	0.14	0.73	0.36	0.89	0.51	0.42	0.41	0.24	0.18	0.26	0.22	11.41	0.40
%STD	0.68	2.24	4.70	5.27	1.14	1.73	1.81	0.52	1.75	0.58	2.36	2.28	3.58	2.73	2.74	2.33	6.08	2.28
intented	76.40	20.00				8.20	40.00	70.00	50.00	90.00	18.00	18.00	6.50	6.50	9.50	9.50		
dif		0.41				0.05	0.31	-0.33	0.65	-0.62	-0.06	0.02	0.10	-0.02	0.02	0.15	0.06	
abs dif		0.41				0.05	0.31	0.33	0.65	0.62	0.06	0.02	0.10	0.02	0.02	0.15	0.23	

Table A.1: CT specimen dimensions in mm

TNB	H	H1	L	t	a0	G [gr]	avg
1	79.6	73.3	149.4	20.16	6.3	916.7	
2	78.2	70.8	150	19.35	7.4	869.2	
3	76.43	69.3	151.3	19.45	7.13	882.2	
4	77.2	63.7	150.9	19.7	13.5	869.3	
avg	77.86	71.13	150.40	19.67	6.94	884.35	65.20
STD	1.19	1.65	0.74	0.31	0.47	19.41	0.87
%STD	1.52	2.32	0.50	1.59	6.74	2.19	2.53
int	75	65	150				
dif	2.86	6.13	0.40				
abs dif	2.86	6.13	0.40				

Table A.2: STNB specimen dimensions in mm

specimen	Ll	Lr	a0	h	t1	t2
1	74.8	74.4	11	60.5	11.2	11

Table A.3: SCB specimen dimensions in mm

B

closed mould injection casting

(a) Applying release agent

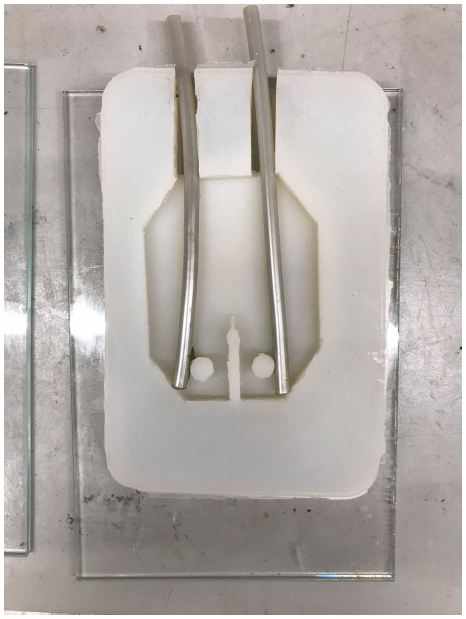

(b) Adding injection tubes

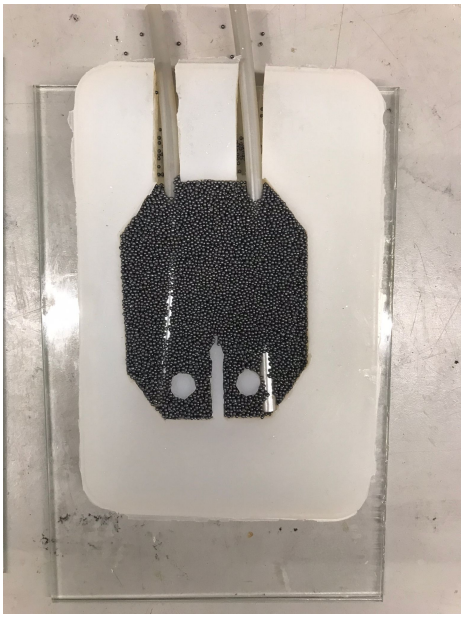

(a) Filling with 190gr steel shot

(b) Clamping of glass cover plate

(a) Moving of injection tubes with resin level

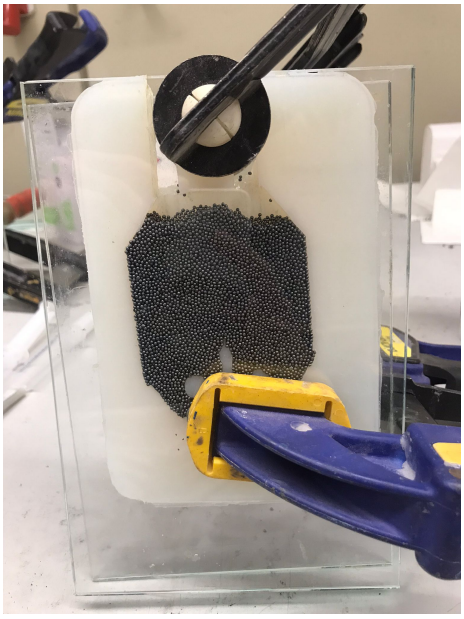

(b) removing injection tubes

(a) topping of steel shot

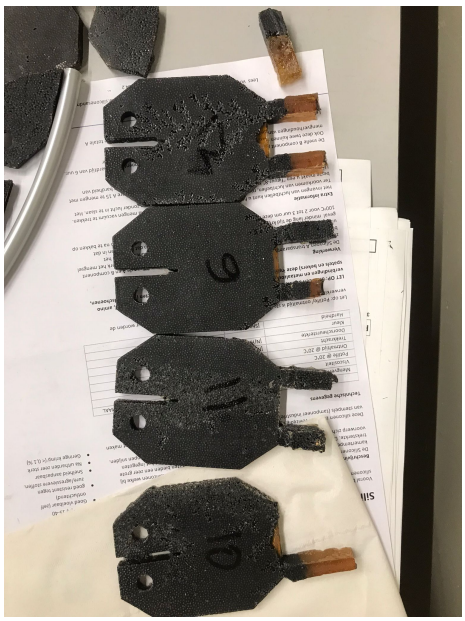

(b) resulting specimens

Figure B.5: end results right edge sawed edges

C

xFEM stress intensity factor values

C.1. CT SIF values

crack length [mm]		Contour 1	Contour 2	Contour 3	Contour 4	Contour 5
15	XFEM 1	533.8	537.9	540.4	545.4	546.3
	XFEM 2	533.8	537.9	540.4	545.4	546.3
25	XFEM 1	882.3	889.7	892.7	899.8	905.7
	XFEM 2	882.3	889.7	892.7	899.8	905.7
30	XFEM 1	1251	1260	1275	1284	1297
	XFEM 2	1251	1260	1275	1284	1297
35	XFEM 1	1994	2008	2030	2051	2085
	XFEM 2	1994	2008	2030	2051	2085

Table C.1: SIF CT mesh size 0.5 mm

crack length [mm]		Contour 1	Contour 2	Contour 3	Contour 4	Contour 5
15	XFEM 1	536	539	538.4	538.7	542.7
	XFEM 2	536	539	538.4	538.7	542.7
25	XFEM 1	867.7	866.3	876.4	881.4	886.3
	XFEM 2	867.7	866.3	876.4	881.4	886.3
30	XFEM 1	1254	1254	1261	1263	1270
	XFEM 2	1254	1254	1261	1263	1270
35	XFEM 1	2080	2064	2062	2066	2076
	XFEM 2	2080	2064	2062	2066	2076

Table C.2: SIF CT mesh size 0.25 mm

crack length [mm]		Contour 1	Contour 2	Contour 3	Contour 4	Contour 5
15	XFEM 1	534.6	533.6	535.1	536.6	538.2
	XFEM 2	534.6	533.6	535.1	536.6	538.2
25	XFEM 1	860.8	873.4	879.2	884.3	888.4
	XFEM 2	860.8	873.4	879.2	884.3	888.4
30	XFEM 1	1241	1247	1251	1256	1262
	XFEM 2	1241	1247	1251	1256	1262
35	XFEM 1	2038	2015	2009	2015	2024
	XFEM 2	2038	2015	2009	2015	2024

Table C.3: SIF CT mesh size 0.1 mm

crack length [mm]		Contour 1	Contour 2	Contour 3	Contour 4	Contour 5
15	XFEM 1	532.6	539.4	542.1	542.1	553
	XFEM 2	532.6	539.4	542.1	542.1	553
25	XFEM 1	882.9	903.1	905	907.6	911.8
	XFEM 2	882.9	903.1	905	907.6	911.8
30	XFEM 1	1260	1269	1284	1298	1322
	XFEM 2	1260	1269	1284	1298	1322
35	XFEM 1	1999	2022	2064	2093	2137
	XFEM 2	1999	2022	2064	2093	2137

Table C.4: SIF CT mesh size 1 mm

crack length [mm]		Contour 1	Contour 2	Contour 3	Contour 4	Contour 5
15	XFEM 1	507	536.7	540.9	540.7	573.8
	XFEM 2	507	536.7	540.9	540.7	573.8
25	XFEM 1	857.9	881.3	887.5	896.1	914.2
	XFEM 2	857.9	881.3	887.5	896.1	914.2
30	XFEM 1	1253	1284	1305	1322	1349
	XFEM 2	1253	1284	1305	1322	1349
35	XFEM 1	1955	2001	2040	2084	2167
	XFEM 2	1955	2001	2040	2084	2167

Table C.5: SIF CT mesh size 2 mm

C.2. 2TCT SIF values

crack length [mm]		Contour 1	Contour 2	Contour 3	Contour 4	Contour 5
25	XFEM 1	272.8	283.2	283.4	281.4	281.2
	XFEM 2	281.5	272.9	280.1	282.2	283.2
35	XFEM 1	366	365.8	365.3	366.3	370.2
	XFEM 2	366	365.8	365.3	366.3	370.2
55	XFEM 1	905.6	906.8	906.3	914.7	916.7
	XFEM 2	905.6	906.8	906.3	914.7	916.7
65	XFEM 1	2338	2340	2351	3099	3767
	XFEM 2	2338	2340	2351	3099	3767

Table C.6: SIF 2TCT mesh size 0.5 mm

C.3. STNB SIF values

crack length [mm]		Contour 1	Contour 2	Contour 3	Contour 4	Contour 5
15	XFEM 1	27.29	27.97	27.61	28.19	27.77
	XFEM 2	27.94	27.73	27.64	27.68	27.4
	XFEM 3	27.84	27.59	27.64	27.9	27.38
	XFEM 4	27.29	27.97	27.61	28.19	27.77
25	XFEM 1	37.32	37.88	38.22	38.28	38.41
	XFEM 2	38.35	38.1	37.95	37.83	37.93
	XFEM 3	38.23	38.12	37.93	37.87	37.89
	XFEM 4	37.32	37.88	38.22	38.28	38.41
45	XFEM 1	81.45	82.2	83.09	83.93	84.2
	XFEM 2	84.35	83.31	82.93	83.11	83.15
	XFEM 3	84.12	83.34	83.01	83.18	83.21
	XFEM 4	81.45	82.2	83.09	83.93	84.2
60	XFEM 1	234.6	240.8	243.6	245.5	246.6
	XFEM 2	242	241.3	240.6	241.9	242.7
	XFEM 3	242.1	241.6	240.8	241.6	243.2
	XFEM 4	234.6	240.8	243.6	245.5	246.6

Table C.7: SIF STNB mesh size 0.5 mm